

# Quantum capacitive coupling between large-angle twisted graphene layers

**Alina Mreńca-Kolasińska<sup>1,2</sup>, Peter Rickhaus<sup>3</sup>, Giulia Zheng<sup>3</sup>, Klaus Richter<sup>4</sup>, Thomas Ihn<sup>3</sup>, Klaus Ensslin<sup>3</sup> and Ming-Hao Liu<sup>1</sup>**

<sup>1</sup> Department of Physics, National Cheng Kung University, Tainan 70101, Taiwan

<sup>2</sup> AGH University of Science and Technology, Faculty of Physics and Applied Computer Science, al. Mickiewicza 30, 30-059 Kraków, Poland

<sup>3</sup> Solid State Physics Laboratory, ETH Zürich, CH-8093 Zürich, Switzerland

<sup>4</sup> Institut für Theoretische Physik, Universität Regensburg, D-93040 Regensburg, Germany

E-mail: minghao.liu@phys.ncku.edu.tw, alina.mrenca@fis.agh.edu.pl

## Abstract.

Large-angle twisted bilayer graphene (tBLG) is known to be electronically decoupled due to the spatial separation of the Dirac cones corresponding to individual graphene layers in the reciprocal space. The close spacing between the layers causes strong capacitive coupling, opening possibilities for applications in atomically thin devices. Here, we present a self-consistent quantum capacitance model for the electrostatics of decoupled graphene layers, and further generalize it to deal with decoupled tBLG at finite magnetic field and large-angle twisted double bilayer graphene at zero magnetic field. We probe the capacitive coupling through the conductance, showing good agreement between simulations and experiments for all the systems considered. We also propose a new experiment utilizing the decoupling effect to induce a huge and tunable bandgap in bilayer graphene by applying a moderately low bias. Our model can be extended to systems composed of decoupled graphene multilayers as well as non-graphene systems, opening a new realm of quantum-capacitively coupled materials.

*Keywords:* twisted bilayer graphene, double twisted bilayer graphene, quantum capacitance

Recently, there has been an increasing interest in thin van der Waals heterostructures [1, 2], including twisted bilayer graphene (tBLG). In tBLG [figure 1(a)], the Brillouin zones of the two layers are rotated against each other [figure 1(b)], and a large twist angle leads to the separation of the Dirac cones of both layers [3, 4, 5, 6, 7]. This suppresses interlayer scattering due to the large momentum difference, making the two layers essentially electronically decoupled [8, 9, 10, 11, 12]. However, their atomically thin layer spacing allows them to couple electrostatically because the electric charge on one layer causes an effective gating of the other layer. This mechanism enables realization of atomically thin devices composed of decoupled layers, with the large twist being an alternative to isolating the layers with dielectrics [13, 14, 15, 16, 17]. However, the strong quantum capacitive coupling makes precise electrostatic modeling indispensable for simulation of these devices [18, 19].

In this work, we present the self-consistent quantum capacitance model used in reference [7] for decoupled tBLG at zero magnetic field and generalize it considerably to deal with decoupled tBLG in the presence of magnetic field, decoupled twisted double Bernal-stacked bilayer graphene (tdBLG), and decoupled multilayer graphene systems. The quantum conductance of such layered structures depends strongly on the capacitive coupling and can be used as a sensitive probe of the latter. We show quantitatively good agreement with our own experimental results for a dual-gated two-terminal tBLG device sketched in Figs. 1(c) and (d), showing strong reliability of our model. For tdBLG, our transport simulations agree well with the experimental findings [20], despite the strong complication due to the gate-tunable band gap [21, 22, 23, 24, 25, 26]. We also propose employing the decoupling mechanism to build a thin capacitor composed of three Bernal-stacked bilayers (BLGs) brought close to each other at a large rotation angle, where the outer ones play the role of the electrostatic gates. Thanks to the large capacitance between the BLGs, and a resulting large bias, it is possible to induce a large bandgap in the middle BLG and investigate the transport features occurring close to the band edge. Our models can be in general applied to electronically decoupled materials that are quantum-capacitively coupled to each other, including topological insulator surface states [27], but is not limited to alike layers, being adaptable to hybrid systems consisting of different materials hosting two-dimensional electron gas [28].

## 1. Methods

*Self-consistent quantum capacitance model for tBLG.* To model the decoupled tBLG device, we assume two layers of graphene described by the linear Dirac dispersion relation  $E = \pm \hbar v_F k$ , where  $\hbar$  is the reduced Planck constant and  $v_F \approx 10^6 \text{ m} \cdot \text{s}^{-1}$  is the Fermi velocity of graphene. We adopt  $\hbar v_F \approx 3\sqrt{3}/8 \text{ eV} \cdot \text{nm}$ . The two electronically decoupled single-layer graphene (SLG) flakes are tightly spaced (assuming the spacing to be  $d_G = 0.12 \text{ nm}$  found in reference [7]) such that a tiny shift of the Fermi energy of the first layer causes an appreciable gating effect on the second layer, which in turn acts as a back gate of the first one. The whole process is iterated using the formulas derived in [29]. The carrier density

$$n = n_C + \Delta n \quad (1)$$

of a SLG free of intrinsic doping and subject to two gates at voltages  $V_1$  and  $V_2$  is composed of the classical carrier density

$$n_C = \sum_{i=1,2} \frac{C_{iG}}{e} V_i, \quad (2)$$

where  $e > 0$  is the elementary charge and  $C_{iG}$  is the capacitance (per unit area) between gate  $i$  and graphene, and the correction

$$\Delta n = \text{sgn}(n_C) n_Q \left( 1 - \sqrt{1 + 2 \frac{|n_C|}{n_Q}} \right) \quad (3)$$

accounting for the quantum nature of the finite density of states of the conducting plate, where

$$n_Q = \frac{\pi}{2} \left( \frac{\hbar v_F}{e} \frac{C_{1G} + C_{2G}}{e} \right)^2 \quad (4)$$

arizes solely from the quantum capacitance [30, 18]. The corresponding electric potential of the graphene sheet is given by

$$V_G = -\frac{e \Delta n}{C_{1G} + C_{2G}}. \quad (5)$$

To apply Eqs. 1–5 to the dual-gated decoupled tBLG device sketched in figure 1(d), we consider the top graphene layer (upper dashed line) to be dual-gated by the top gate at voltage  $V_t$  and bottom graphene layer (lower dashed line) at electric potential  $V_{Gb}$ . Substituting  $V_1 = V_t$ ,  $V_2 = V_{Gb}$ ,  $C_{1G} = C_t$ , and  $C_{2G} = C_g$  into Eqs. 2–5, we obtain the electric potential  $V_{Gt}$  of the top graphene layer, given  $V_t$  and  $V_{Gb}$ , the former being a fixed input while the latter to be self-consistently iterated. Similarly, the bottom graphene layer is dual-gated by the top

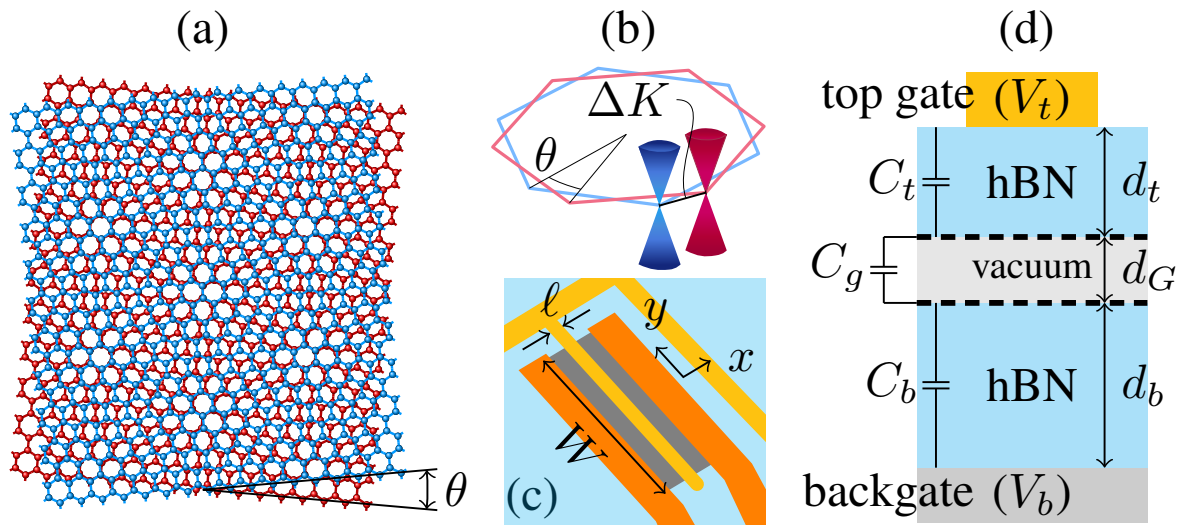


**Figure 1. The tBLG device design.** Schematics of (a) a tBLG lattice composed of two graphene layers twisted by an angle  $\theta$  and (b) their corresponding Dirac cones in reciprocal space. The dual-gated two-terminal decoupled tBLG device considered in the transport experiment and simulations is sketched in (c) for a perspective top view and (d) for its side view.

graphene layer at potential  $V_{Gt}$  and back gate at voltage  $V_b$ . Substituting  $V_1 = V_{Gt}$ ,  $V_2 = V_b$ ,  $C_{1G} = C_g$ , and  $C_{2G} = C_b$  into Eqs. 2–5, we obtain the electric potential  $V_{Gb}$  of the bottom graphene layer, given  $V_{Gt}$  and  $V_b$ , the former being just computed and the latter being a fixed input. The newly obtained  $V_{Gb}$  is used to compute  $V_{Gt}$  and vice versa iteratively, until  $V_{Gt}$  and  $V_{Gb}$  both converge to a satisfactory precision. From the converged  $V_{Gt}$  and  $V_{Gb}$  one obtains the individual carrier density  $n_t$  ( $n_b$ ) for the top (bottom) layer, using Eqs. 1–4. Then,  $-eV_{Gt}$  and  $-eV_{Gb}$  are the onsite energies entering the tight-binding Hamiltonian for transport calculations to be explained later. The capacitance and intrinsic doping can in general be position-depent,  $C_t = C_t(x)$ , and the convergence is required for all  $x$ , leading all  $n_t, n_b, V_{Gt}, V_{Gb}$  to depend on  $x$ . For capacitance  $C = C(x, y)$  the same requirement applies for all relevant  $x$  and  $y$ , but in each case the iteration converges rapidly.

For strong magnetic field we account for the Landau quantization of the density of states,  $D(E, B_z) = \frac{4eB_z}{h} \sum_{n_L} \delta(E - E_{n_L})$ , where  $E_{n_L} = \text{sgn}(n_L) \sqrt{2eB_z \hbar v_F^2 |n_L|}$  and  $n_L = 0, \pm 1, \pm 2, \dots$ . The carrier density is given by

$$n(E, B_z) = \int_0^E D(E', B_z) dE'. \quad (6)$$

To account for the Landau level (LL) broadening, we approximate the Dirac delta by a Lorentzian function, and the integration (6) can be done analytically. The resulting carrier density is quantized in energy and magnetic field. The carrier density given by equation (6) is equal to the sum of the gate-induced doping

$$n(eV_G, B_z) = \frac{C_{1G}}{e}(V_1 - V_G) + \frac{C_{2G}}{e}(V_2 - V_G). \quad (7)$$

We solve equation (7) for  $V_G$  numerically. Then, for two decoupled graphene layers in strong external magnetic field, the calculation of the electric potential  $V_{Gt}$  and  $V_{Gb}$  is done in a similar self-consistent way as for the linear dispersion relation but substituting equations (1)–(5) with the numerical solution of equation (7) (for details see the Supplemental Materials [31]).

*Quantum capacitance model for tDBG.* We first develop a quantum capacitance model for an individual dual-gated BLG based on Refs. [32, 33]. We consider a general case with the onsite energy given by  $U_0 \pm U/2$  for the top (bottom) layer, where  $U$  is the asymmetry parameter and  $U_0 = -eV_G$  is the band offset.

The relation between the carrier density, the asymmetry parameter, and the band offset is given by [34]

$$-eV_G = -\text{sgn}(n) \sqrt{\frac{\gamma_1^2}{2} + \frac{U^2}{4} + \hbar^2 v_F^2 \pi |n|} - \frac{\gamma_1}{2} \sqrt{\gamma_1^2 + (2\hbar v_F)^2 \pi |n| \left(1 + \frac{U^2}{\gamma_1^2}\right)}. \quad (8)$$

For a dual gated sample, and the densities of the top and bottom layer given by  $n_t$  and  $n_b$ , respectively, we obtain

$$n_b - n_t = -\frac{n_\perp U}{2\gamma_1} \ln \left( \frac{|n|}{2n_\perp} + \frac{1}{2} \sqrt{\left(\frac{n}{n_\perp}\right)^2 + \left(\frac{U}{2\gamma_1}\right)^2} \right), \quad (9)$$

$$n_b - n_t = \frac{C_b}{e} \left[ V_b - \left( V_G + \frac{U}{2e} \right) \right] - \frac{C_t}{e} \left[ V_t - \left( V_G - \frac{U}{2e} \right) \right] - \frac{2C_g U}{e e}, \quad (10)$$

$$n = n_b + n_t = \frac{C_b}{e} V_b + \frac{C_t}{e} V_t - \frac{C_b + C_t}{e} V_G + \frac{C_t - C_b}{e} \frac{U}{2e}, \quad (11)$$

where  $\gamma_1 = 0.39$  eV is the nearest-neighbor hopping for the interlayer coupling, and  $n_\perp = \gamma_1^2 / \pi \hbar^2 v_F^2$  is the characteristic carrier density. For the details of the derivation see reference [31]. The system of four nonlinear equations (8 – 11) is solved numerically to obtain  $\Delta n = n_t - n_b$ ,  $n = n_t + n_b$ ,  $U$ , and  $V_G$ .

With the quantum capacitance model for BLG at hand, we can further extend it to tdBLG. To this end, we consider two stacked BLGs, coupled capacitively to external top and bottom gates and to each other [see figure 4(c)]. The problem can be then solved self-consistently as for tBLG; however, we found treating the problem as a set of eight coupled nonlinear equations more efficient (see [31]).

*Quantum transport calculation.* To simulate real devices and speed up calculations, the hopping parameter  $t_0$  and lattice spacing  $a_0$  approximated by 3 eV and  $1/4\sqrt{3}$  nm, respectively, are scaled to  $t_0/s_f$  and  $s_f a_0$  [35] using  $s_f = 4$  (only for BLG and tdBLG we use  $s_f = 2$ ). We express the two-terminal conductance as  $G = (R_c + G_0^{-1})^{-1}$ , where  $R_c$  is the contact resistance and  $G_0$  is the ballistic conductance calculated using the real-space Green's function approach [36]. For tBLG devices at zero or low magnetic field, we use  $R_c = 0.005 h/e^2$  as a reasonable parameter for the contact resistance. Here, as well as for tdBLG we assume the system is translationally invariant along the lateral direction, and  $G_0$  is computed by using the method of periodic boundary hopping [37, 38, 39]:  $G_0 = (W/3\pi s_f a_0)(g_b + g_t)$ , where  $g_j = (e^2/h) \int_{-k_F}^{k_F} T(k_y) dk_y$  ( $k_F$  being the Fermi momentum) [40] is the normalized conductance of the bottom (top) graphene layer for  $j = b$  ( $j = t$ ). The system is described by the tight-binding Hamiltonian

$$H_j = H_0 - e \sum_n V_{Gj}(x_n) c_n^\dagger c_n, \quad (12)$$

where  $j = t, b$  is the layer index,  $H_0$  is the clean part of the minimal tight-binding model for bulk graphene [38, 39], and the operator  $c_n$  ( $c_n^\dagger$ ) annihilates (creates) an electron on site  $n$  located at  $(x_n, y_n)$ . It is the second term in equation (12) for the onsite energy where the electric potential  $V_{Gb}$  and  $V_{Gt}$ , found from the self-consistent electrostatic model, enter the transport calculations.

For the transport modeling of tBLG at large magnetic field we use the wave-function matching method [41] for graphene, considering a zigzag ribbon of width 400 nm. At zero-temperature the conductance is calculated using the Landauer formula  $G(B) = 2e^2 T(B)/h$ , with  $T(B)$  being the transmission summed over all modes.

## 2. Results

*Self-consistent quantum capacitance model for decoupled tBLG.* Reference [7] investigated dual-gated two-terminal devices consisting of decoupled large-angle tBLG samples,

schematically shown in figure 1(c) for a perspective top view and in figure 1(d) for its side view. In the following discussion we focus on a device fabricated with a top gate of length  $\ell = 320$  nm and sample width  $W \approx 2.9$   $\mu$ m. Details of the device fabrications are given in reference [7].

*Decoupled tBLG without magnetic field.* We assume the two layers of graphene without magnetic field are described by the linear Dirac dispersion relation. Figure 2(a) shows the computed two-terminal conductance simulated for the considered decoupled tBLG device sketched in Figs. 1(c)–(d) as a function of  $V_t$  and  $V_b$ . The diagonal charge neutrality line splits into two which is a signature of the decoupling of the two graphene layers. The splitting as well as the superimposed Fabry-Pérot (FP) interference fringes [42, 43] are better seen by mean of numerical differentiation. We show  $dg/dV_t$  as an overlaid inset on figure 2(a), where the horizontally aligned dots mark the scan with  $3\text{ V} \leq V_t \leq 5\text{ V}$  at  $V_b = -10\text{ V}$  that we are going to focus on for the rest of the discussions of the decoupled tBLG device. Along this  $V_t$  scan, the carrier density profiles  $n_b(x)$  and  $n_t(x)$  are shown in figure 2(b) and (c), respectively. The  $V_t$  dependence of  $n_b(0)$  and  $n_t(0)$  is shown in figure 2(d), where three regions can be clearly seen: Both graphene layers in unipolar ppp for  $V_t \lesssim 3.6\text{ V}$ , top layer in pnp but bottom layer remaining in ppp for  $3.6\text{ V} \lesssim V_t \lesssim 4.5\text{ V}$ , and both layers in pnp for  $V_t \gtrsim 4.5\text{ V}$ . These regions are characterized by no FP fringes, one set of FP fringes and two sets of FP fringes, respectively.

*Decoupled tBLG with magnetic field.* We next go beyond reference [7] to account for magnetotransport in the same decoupled tBLG device, where the uniform magnetic field  $B$  is applied along  $z$  perpendicular to the graphene layers. When  $B$  is weak, the Dirac linear dispersion remains valid, and the above introduced self-consistent model can be directly applied. Figure 2(e) shows the experimentally measured two-terminal conductance  $G$  as a function of  $V_t$  restricted to the range marked in figure 2(a) and  $B$  up to 0.3 T. Our simulated  $G$  shown in figure 2(f) exhibits a similar profile, despite the different magnitude of  $G$ . To better compare the details with our simulation, we mirror the experimental data about the  $V_t$  axis and show  $dG/dV_t$  in figure 2(g). It exhibits complex FP fringes that are satisfactorily consistent with our computed differentiated normalized conductance  $dg/dV_t$  shown in figure 2(h). Closer inspection of the region with  $V_t \gtrsim 4.5\text{ V}$  shows that there are two sets of FP fringes superimposed, one dispersing with  $B$  slower and the other faster. The slower (faster) set is expected to come from the top (bottom) graphene layer because of the higher (lower) gating efficiency; the layer with lower gating efficiency needs a larger gate voltage to compete with the  $B$ -dependent Aharonov-Bohm phase picked up by the interfering electron within the FP cavity [44]. This is confirmed by showing the individual contribution  $g_b$  and  $g_t$  in figure 2(i) and (j), respectively, which sum up to  $g = g_b + g_t$ .

Next we turn to strong external magnetic field. Figure 3(a) shows the experimentally measured and figure 3(b) the calculated transconductance obtained at  $V_b = -10\text{ V}$  as a function of the top-gate voltage and magnetic field. In the transconductance map, two sets of Landau levels are visible, emerging from the two split charge neutrality points, marked



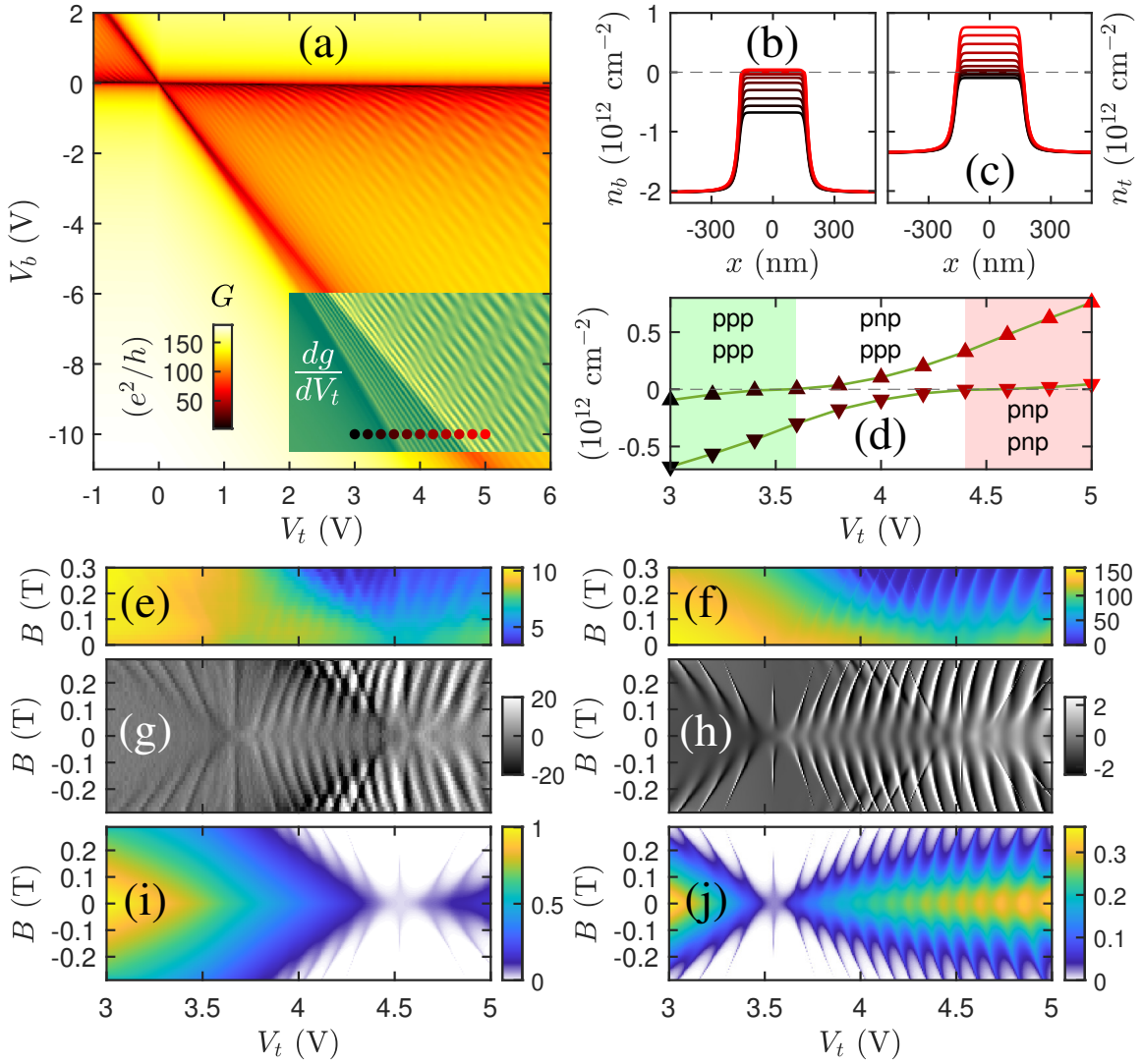


**Figure 2.**  $B = 0$  to low  $B$ . (a) Calculated two-terminal conductance  $G$  as a function of top gate voltage  $V_t$  and back gate voltage  $V_b$  at zero magnetic field  $B = 0$ . The overlay at the bottom right corner shows the numerical derivative of the normalized conductance  $g$  with respect to  $V_t$ . Carrier density profiles  $n_b(x)$  and  $n_t(x)$  of the bottom and top graphene layer are shown in (b) and (c), respectively, subject to gate voltage configurations marked in (a) with the line and dot colors corresponding to each other. (d)  $n_b(x=0)$  and  $n_t(x=0)$  marked by  $\nabla$  and  $\triangle$  as a function of  $V_t$  at fixed  $V_b = -10$  V corresponding to panel (b) and (c), respectively. Shaded areas distinguish three regions: both layers in ppp (light green), top layer in pnp but bottom layer in ppp (white), and both layers in pnp (pink). (e) Measured and (f) simulated two-terminal conductance  $G$  as functions of  $V_t$  and  $B$  up to 0.3 T. Fabry-Pérot interference fringes of  $dG/dV_t$  from the experiment and  $dg/dV_t$  from the simulations are shown in (g) and (h), respectively. Calculated normalized conductance  $g$  for the (i) bottom and (j) top graphene layer. Color bars are in units of  $e^2/h$  for (e), (f), (i), and (j), and  $e^2/h \text{ V}^{-1}$  for (g) and (h).

by red arrows in figure 3(a) and (b). The individual top and bottom layer conductances are shown in figure 3(c) and (d), respectively, confirming that the entire LL spectrum consists of two layers' superimposed Landau fans, and that the layers remain electrically decoupled

at strong magnetic field. The Landau fans are dramatically different from the commonly observed ones in graphene, and exhibit "kinks" at the crossing between the Landau levels of the two layers. Their origin can be understood by comparing the conductance map to the top and bottom layer density gradient with respect to  $V_t$  in figure 3(e), and (f), respectively.

We first focus on the 2nd, 3rd, and 4th LL of the bottom layer marked by squares in figure 3(d). The density of states (DoS) is high at the LL, as is the density per gate voltage. Thus, the  $dn_b/dV_t$  value is high, [figure 3(f)] and the  $dn_t/dV_t$  value [figure 3(e)] is low as the total carrier density induced by the top gate is conserved. On the other hand, the points marked with circles in figure 3(d), (e) and (f) are along the top layer 0th LL, and the top layer DoS is high. Based on the argument above, here the  $dn_t/dV_t$  ( $dn_b/dV_t$ ) value is high (low). Therefore, we expect the slope of the LLs to change, and in particular at the points marked with circles, the bottom layer LLs slope becomes smaller. Recent experiment [12] reported similar effects. Note that this feature is only recovered in the LL-quantized-density model. For the result obtained with the linear dispersion relation see [31]. The good qualitative agreement between

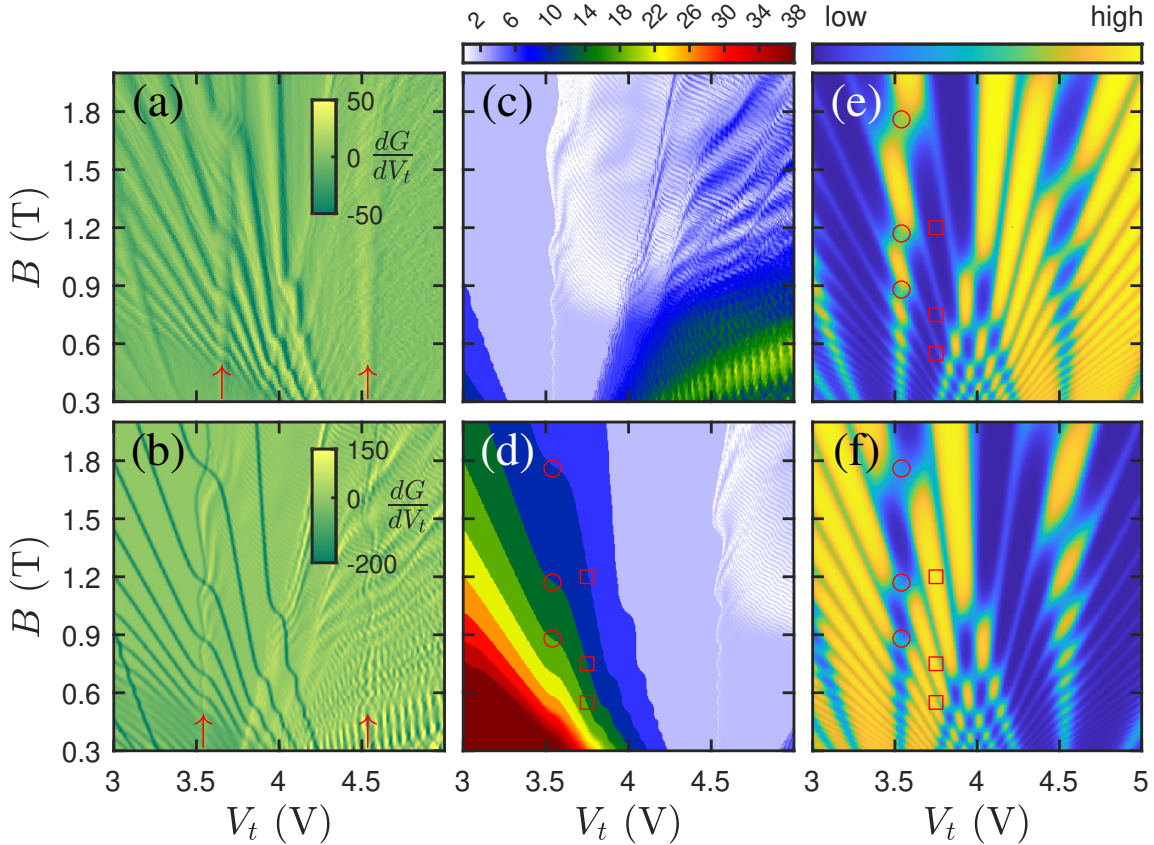


**Figure 3. Strong magnetic field transport in tBLG.** Numerical derivative of the (a) measured and (b) calculated two-terminal conductance as a function of top gate voltage  $V_t$  and magnetic field at  $V_b = -10$  V. (c), (d) Individual conductances calculated for the top and bottom layer, respectively. (e)  $dn_t/dV_t$  and (f)  $dn_b/dV_t$  values show a clear correspondence to the conductance plateaus kinks.



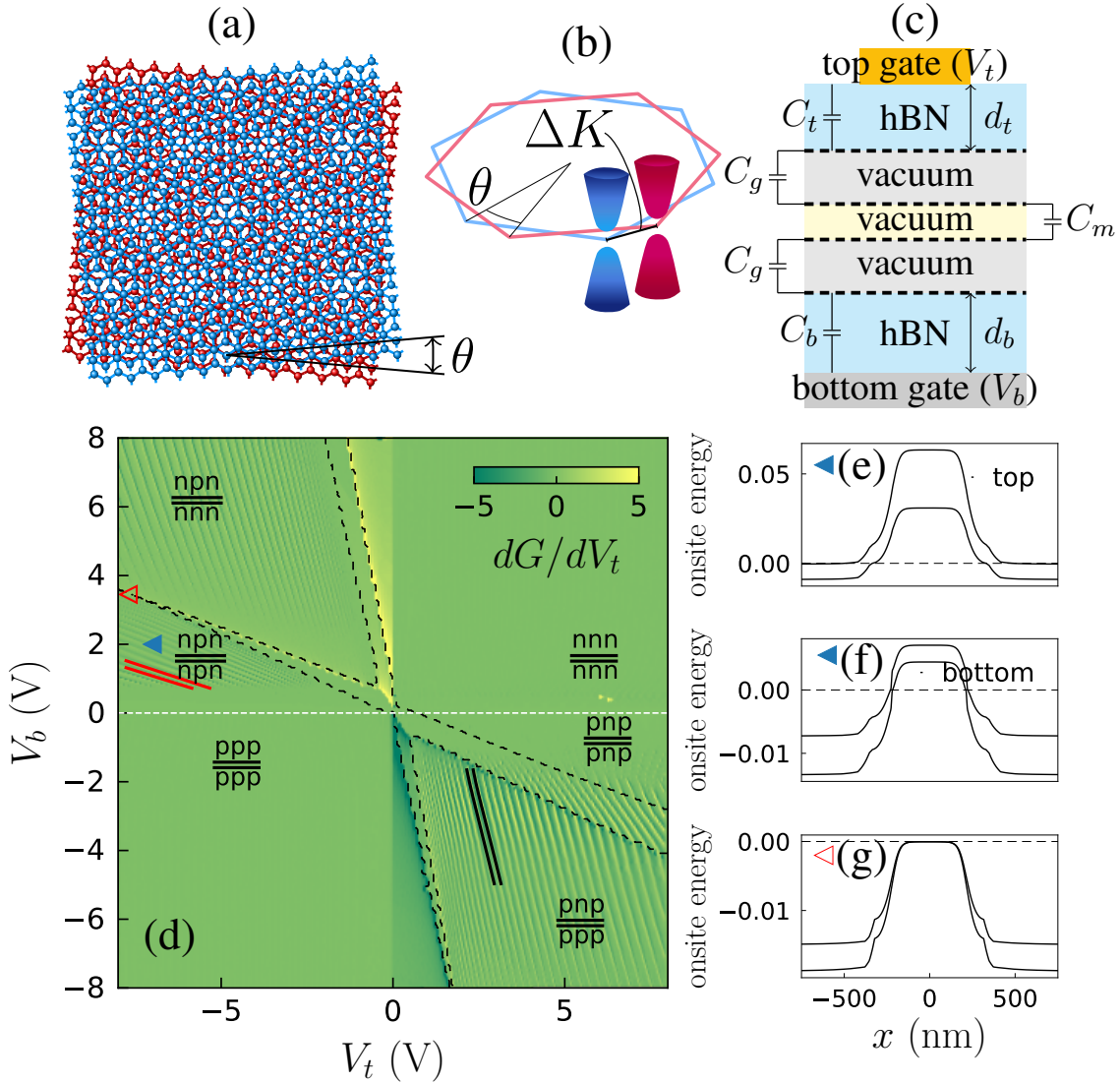


**Figure 4. Fabry-Pérot oscillation in tdBLG.** (a) Sketch of the Bernal stacked large-angle tdBLG and (b) its low-energy bandstructure. (c) Schematic of the dual-gated tdBLG system. (d) Numerical derivative of two-terminal conductance as a function of top gate and back gate voltage in tdBLG. The onsite energy profiles at the voltage configuration marked by  $\blacktriangleleft$  are shown in (e) for the top BLG and (f) and (g) for the bottom BLG.

the experimental and theoretical results shows that the self-consistent model is accurate for other than linear dispersion relations.

*Decoupled tdBLG.* We next consider large-angle tdBLG [figure 4(a)], where, similar to the tBLG case, the two BLGs are decoupled electronically by the large momentum separation of the Dirac cones of the two BLGs [figure 4(b)].

The gate capacitances  $C_t$ ,  $C_b$  are obtained from a finite element electrostatic simulation for a sample geometry adopted from reference [20], with the hBN thicknesses  $d_b = 90$  nm,  $d_t = 60$  nm, placed between a global back gate and narrow top gate width 400 nm. The

interlayer capacitance within an individual BLG is assumed to be  $C_g = 7.4 \mu\text{Fcm}^{-2}$  [7], whereas the value of the capacitance between the BLG layers is  $C_m = 3.5 \mu\text{Fcm}^{-2}$  [20].

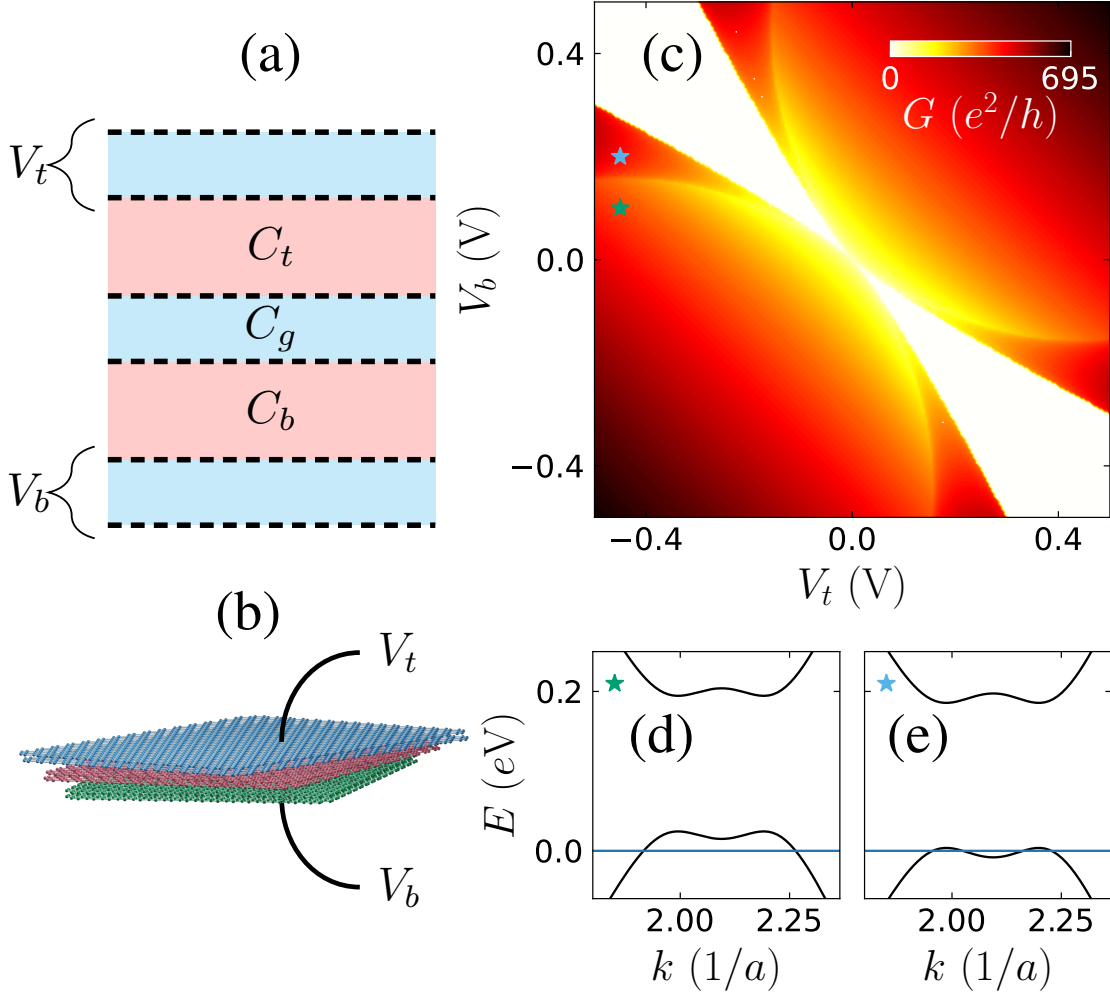
In the self-consistent model for tdBLG, we include the effect of the crystal field [45, 46, 47, 48] which was shown in reference [20] to open a bandgap even without gate voltage. In the tdBLG sample the inner and outer graphene layers see a different environment, and thus feel an unequal electrostatic potential, which effectively creates an intrinsic bias. This induces a small negative charge in the inner layers. We can include this effect in our model by assuming a constant density difference  $\Delta n_0$  between the bottom and top layer of a BLG. From the measured values of the displacement field needed to close the bandgaps [20] we estimate  $\Delta n_{0,1} = 13 \times 10^{11} \text{cm}^{-2}$  for the upper BLG and  $\Delta n_{0,2} = -14 \times 10^{11} \text{cm}^{-2}$  for the lower BLG.

Figure 4(d) shows the transconductance as a function of  $V_t$  and  $V_b$ , which recovers the key features observed in reference [20]. The FP oscillations occur when a bipolar junction is formed in the top or bottom BLG. Interestingly, for negative  $V_b$  the oscillations occur for the top BLG only (the slope highlighted by black solid lines). Conversely, for  $0 < V_b < 4 \text{ V}$  the FP oscillation is present only for the bottom BLG (highlighted by red lines); at higher  $V_b$  only a faint oscillation for the top BLG can be spotted, when the n-p-n junction is formed in the upper BLG [see labels in figure 4(d)]. This difference in the visibility of the oscillations can be explained as due to a large bandgap across the device, which strongly reduces the transmission through the cavity when the p-n interface is smooth. For example, the oscillation in the top BLG is hardly visible at  $V_b > 0$  where the bandgap at the p-n interface happens to be large [see the onsite energy profile in figure 4 (e)], but in the bottom BLG the bandgap is reduced by the applied displacement field [figure 4 (f)].

Another feature which our model captures in good qualitative agreement with experiment is the bandgaps in the top-gated region that are opened even at low applied gate voltages [shown in figure 4(d) by black dashed lines] and closed at  $(2.2, -10.6)\text{V}$  for the upper BLG and  $(V_t, V_b) \approx (-7.7, 3.4)\text{V}$  for the lower BLG [see figure 4 (g)]. A feature not taken into account by the model is the difference in the electron and hole effective mass leading to a kink of the charge neutrality line in the experiment [20].

*Graphene-gated Bernal stacked bilayer graphene.* Etched graphene can be used to define graphene side gates in planar graphene devices [49, 50]. Here we propose a device based on stacked graphene layers, where the outer layers are used as gates. The decoupling of large-angle twisted graphene layers can be employed to build a thin capacitor with an enormous geometrical capacitance. Thus, a small voltage applied to the top and bottom BLG is sufficient to create a large displacement field between the BLG layers leading to a huge band gap that can be continuously tuned in a very large range, from zero to 200 meV for experimentally accessible parameters.

The proposed setup consists of three stacked BLG flakes, as shown schematically in figure 5(a), where the outer BLGs are twisted at a large angle relative to the middle one. This can be for example achieved by tearing BLG and stacking the pieces at a controlled angle [2, 51, 52]. The topmost and bottom-most bilayers are then contacted separately [figure 5(b)]. We assume  $C_t = C_b = 3.5 \mu\text{Fcm}^{-2}$  [20]. In principle it should also be possible to stack single



**Figure 5. BLG dual gated by twisted top and bottom BLG.** (a) Side view of the device. (b) Cartoon illustrating the design. (c) Conductance of the middle BLG as a function of the top and bottom gate voltages obtained with the quantum capacitance model for an assumed sample width of  $1 \mu\text{m}$ . (d, e) Band structures at the voltage configurations marked by the stars in (b).

layer graphene at an angle on top and bottom of the BLG, however such an approach is more challenging in practice.

Figure 5(c) shows the conductance of the middle BLG as a function of the top and bottom gate voltage. In the present setup the large potential difference leads to opening of a large band gap and a resulting insulating state. This produces a large region of zero conductance near the charge neutrality point. In the map it is possible to spot a distinct conductance dip further from the charge neutrality point, which corresponds to the 'Mexican hat' structure at the band edge [32]. A representative band structure in the regime with the Fermi energy within the Mexican-hat range is shown in figure 5(d), while shifting the Fermi energy out of this range corresponds to crossing the dip [figure 5(e)]. This crossing corresponds to a topological Lifshitz transition which was directly measured only at finite magnetic field in bilayer graphene [53].

*Decoupled multi-layer graphene.* The iterative process can also be applied to a system composed of more graphene layers, provided that each one is twisted by a large angle such that all the layers are electrically decoupled. Such systems have been realized experimentally [54, 55]. For more details on the carrier density in  $n$ -layer graphene see [31].

### 3. Discussion

In conclusion, we developed self-consistent methods for the electrostatic calculations for electronically decoupled graphene multilayers. We fabricated encapsulated twisted bilayer graphene samples, and performed low-temperature transport measurements and quantum transport simulations. For the twisted double bilayer graphene sample described in reference [20] we model the electrostatics and transport. The theoretical and measured conductance show excellent agreement for both tBLG and tdBLG, confirming the accuracy of the model and the extraordinary decoupling between the atomically-close multilayers. Having confirmed the applicability of the quantum capacitance model for bilayer graphene, we also apply it to design a dual-gated BLG device that uses the decoupling mechanism to create a thin capacitor, which allows for the observation of a very large and entirely tuneable energy gap in BLG. Our results show that the decoupling in large-angle twisted graphene systems can be exploited to investigate the band structure in BLG close to the band edge, which in practice includes also the trigonal warping effect that is theoretically captured when the skew interlayer hopping is included in the BLG Hamiltonian. The decoupling can also be employed in decoupled multi-layer graphene, where the sheets retain the remarkable mobility of single layer graphene, while conducting in multiple parallel planes. Such high-mobility, ultra-thin devices open doors for various applications in electronics.

The good agreement with the experimentally measured conductance for tBLG and tdBLG suggests their applicability is not limited to graphene-based devices, but also for a broad class of systems consisting of decoupled conducting layers. The self-consistent method is suitable to other materials hosting Dirac carriers, for example topological insulator surface states, as well as described by other band structures [27], opening a new area of capacitively-coupled materials.

### Acknowledgments

This work was supported by the Ministry of Science and Technology grant MOST 109-2811-M-006-544. KR acknowledges funding through the Deutsche Forschungsgemeinschaft (DFG, German Research Foundation) Project-ID No. 314695032–SFB 1277 (subproject A07). This research was supported in part by PL-Grid Infrastructure.

### References

- [1] Geim A K and Grigorieva I V 2013 *Nature* **499** 419–425 ISSN 1476-4687 URL <https://doi.org/10.1038/nature12385>

- [2] Kim K, Yankowitz M, Fallahazad B, Kang S, Movva H C P, Huang S, Larentis S, Corbet C M, Taniguchi T, Watanabe K, Banerjee S K, LeRoy B J and Tutuc E 2016 *Nano Lett.* **16** 1989–1995 ISSN 1530-6984 URL <https://doi.org/10.1021/acs.nanolett.5b05263>
- [3] Fallahazad B, Hao Y, Lee K, Kim S, Ruoff R S and Tutuc E 2012 *Phys. Rev. B* **85**(20) 201408(R) URL <https://link.aps.org/doi/10.1103/PhysRevB.85.201408>
- [4] Luican A, Li G, Reina A, Kong J, Nair R R, Novoselov K S, Geim A K and Andrei E Y 2011 *Phys. Rev. Lett.* **106**(12) 126802 URL <https://link.aps.org/doi/10.1103/PhysRevLett.106.126802>
- [5] Sanchez-Yamagishi J D, Taychatanapat T, Watanabe K, Taniguchi T, Yacoby A and Jarillo-Herrero P 2012 *Phys. Rev. Lett.* **108**(7) 076601 URL <https://link.aps.org/doi/10.1103/PhysRevLett.108.076601>
- [6] Sanchez-Yamagishi J D, Luo J Y, Young A F, Hunt B M, Watanabe K, Taniguchi T, Ashoori R C and Jarillo-Herrero P 2017 *Nat Nano* **12** 118–122 ISSN 1748-3395 URL <https://doi.org/10.1038/nnano.2016.214>
- [7] Rickhaus P, Liu M H, Kurpas M, Kurzmann A, Lee Y, Overweg H, Eich M, Pisoni R, Taniguchi T, Watanabe K, Richter K, Ensslin K and Ihn T 2020 *Science Advances* **6** eaay8409 URL <https://www.science.org/doi/abs/10.1126/sciadv.aay8409>
- [8] Schmidt H, Lüdtkke T, Barthold P, McCann E, Fal'ko V I and Haug R J 2008 *Appl. Phys. Lett.* **93** 172108 URL <https://doi.org/10.1063/1.3012369>
- [9] Schmidt H, Lüdtkke T, Barthold P and Haug R J 2010 *Phys. Rev. B* **81**(12) 121403(R) URL <https://link.aps.org/doi/10.1103/PhysRevB.81.121403>
- [10] Kim Y, Yun H, Nam S G, Son M, Lee D S, Kim D C, Seo S, Choi H C, Lee H J, Lee S W and Kim J S 2013 *Phys. Rev. Lett.* **110**(9) 096602 URL <https://link.aps.org/doi/10.1103/PhysRevLett.110.096602>
- [11] Deng B, Wang B, Li N, Li R, Wang Y, Tang J, Fu Q, Tian Z, Gao P, Xue J and Peng H 2020 *ACS Nano* **14** 1656–1664 ISSN 1936-0851 URL <https://doi.org/10.1021/acsnano.9b07091>
- [12] Piccinini G, Miseikis V, Watanabe K, Taniguchi T, Coletti C and Pezzini S 2021 Parallel transport and layer-resolved thermodynamic measurements in twisted bilayer graphene (*Preprint* 2109.06812)
- [13] Kim S, Jo I, Dillen D C, Ferrer D A, Fallahazad B, Yao Z, Banerjee S K and Tutuc E 2012 *Phys. Rev. Lett.* **108**(11) 116404 URL <https://link.aps.org/doi/10.1103/PhysRevLett.108.116404>
- [14] Gorbachev R V, Geim A K, Katsnelson M I, Novoselov K S, Tudorovskiy T, Grigorieva I V, MacDonald A H, Morozov S V, Watanabe K, Taniguchi T and Ponomarenko L A 2012 *Nat. Phys.* **8** 896–901 ISSN 1745-2481 URL <https://doi.org/10.1038/nphys2441>
- [15] Li J I A, Taniguchi T, Watanabe K, Hone J and Dean C R 2017 *Nat. Phys.* **13** 751–755 ISSN 1745-2481 URL <https://doi.org/10.1038/nphys4140>
- [16] Lee K, Jung J, Fallahazad B and Tutuc E 2017 *2D Materials* **4** 035018 URL <https://doi.org/10.1088/2053-1583/aa7bcf>
- [17] Liu X, Hao Z, Watanabe K, Taniguchi T, Halperin B I and Kim P 2019 *Nat. Phys.* **15** 893–897 ISSN 1745-2481 URL <https://doi.org/10.1038/s41567-019-0546-0>
- [18] Fang T, Konar A, Xing H and Jena D 2007 *Applied Physics Letters* **91** 092109 URL <https://doi.org/10.1063/1.2776887>
- [19] Xia J, Chen F, Li J and Tao N 2009 *Nature Nanotechnology* **4** 505–509 ISSN 1748-3395 URL <https://doi.org/10.1038/nnano.2009.177>
- [20] Rickhaus P, Zheng G, Lado J L, Lee Y, Kurzmann A, Eich M, Pisoni R, Tong C, Garreis R, Gold C, Masseroni M, Taniguchi T, Watanabe K, Ihn T and Ensslin K 2019 *Nano Lett.* **19** 8821–8828 URL <https://doi.org/10.1021/acs.nanolett.9b03660>
- [21] McCann E 2006 *Phys. Rev. B* **74**(16) 161403(R) URL <https://link.aps.org/doi/10.1103/PhysRevB.74.161403>
- [22] Castro E V, Novoselov K S, Morozov S V, Peres N M R, Lopes dos Santos J M B, Nilsson J, Guinea F, Geim A K and Neto A H C 2007 *Phys. Rev. Lett.* **99**(21) 216802 URL <https://link.aps.org/doi/10.1103/PhysRevLett.99.216802>
- [23] Oostinga J B, Heersche H B, Liu X, Morpurgo A F and Vandersypen L M K 2008 *Nat. Mater.* **7** 151–157



- ISSN 1476-4660 URL <https://doi.org/10.1038/nmat2082>
- [24] Zhang Y, Tang T T, Girit C, Hao Z, Martin M C, Zettl A, Crommie M F, Shen Y R and Wang F 2009 *Nature* **459** 820–823 ISSN 1476-4687 URL <https://doi.org/10.1038/nature08105>
- [25] Mak K F, Lui C H, Shan J and Heinz T F 2009 *Phys. Rev. Lett.* **102**(25) 256405 URL <https://link.aps.org/doi/10.1103/PhysRevLett.102.256405>
- [26] Taychatanapat T and Jarillo-Herrero P 2010 *Phys. Rev. Lett.* **105**(16) 166601 URL <https://link.aps.org/doi/10.1103/PhysRevLett.105.166601>
- [27] Ziegler J, Kozlov D A, Mikhailov N N, Dvoretzky S and Weiss D 2020 *Phys. Rev. Research* **2**(3) 033003 URL <https://link.aps.org/doi/10.1103/PhysRevResearch.2.033003>
- [28] Simonet P, Rössler C, Krähenmann T, Varlet A, Ihn T, Ensslin K, Reichl C and Wegscheider W 2015 *Applied Physics Letters* **107** 023105 URL <https://doi.org/10.1063/1.4926855>
- [29] Liu M H 2013 *Phys. Rev. B* **87**(12) 125427 URL <https://link.aps.org/doi/10.1103/PhysRevB.87.125427>
- [30] Luryi S 1988 *Applied Physics Letters* **52** 501–503 URL <https://doi.org/10.1063/1.99649>
- [31] See Supplemental Material at ... for details on the self-consistent model with and without Landau quantization, the tBLG magnetoconductance within the linear dispersion relation model, the quantum capacitance model for Bernal-stacked BLG and for tdBLG, the carrier density in multilayer graphene, and the approach for a general band structure
- [32] McCann E and Koshino M 2013 *Rep. Progr. Phys.* **76** 056503 URL <https://doi.org/10.1088/0034-4885/76/5/056503>
- [33] Tomadin A, Carrega M and Polini M 2021 *Phys. Rev. B* **103**(8) 085426 URL <https://link.aps.org/doi/10.1103/PhysRevB.103.085426>
- [34] Varlet A, Liu M H, Krueckl V, Bischoff D, Simonet P, Watanabe K, Taniguchi T, Richter K, Ensslin K and Ihn T 2014 *Phys. Rev. Lett.* **113**(11) 116601 URL <https://link.aps.org/doi/10.1103/PhysRevLett.113.116601>
- [35] Liu M H, Rickhaus P, Makk P, Tóvári E, Maurand R, Tkatschenko F, Weiss M, Schönenberger C and Richter K 2015 *Phys. Rev. Lett.* **114**(3) 036601 URL <https://link.aps.org/doi/10.1103/PhysRevLett.114.036601>
- [36] Datta S 1995 *Electronic Transport in Mesoscopic Systems* (Cambridge University Press, Cambridge)
- [37] Wimmer M 2008 *Quantum transport in nanostructures: From computational concepts to spintronics in graphene and magnetic tunnel junctions* Ph.D. thesis Universität Regensburg
- [38] Liu M H and Richter K 2012 *Phys. Rev. B* **86**(11) 115455 URL <https://link.aps.org/doi/10.1103/PhysRevB.86.115455>
- [39] Liu M H, Bundesmann J and Richter K 2012 *Phys. Rev. B* **85**(8) 085406 URL <https://link.aps.org/doi/10.1103/PhysRevB.85.085406>
- [40] Kang W H, Chen S C and Liu M H 2020 *Phys. Rev. B* **102** 195432
- [41] Kolasiński K, Szafran B, Brun B and Sellier H 2016 *Phys. Rev. B* **94**(7) 075301 URL <https://link.aps.org/doi/10.1103/PhysRevB.94.075301>
- [42] Young A F and Kim P 2009 *Nat. Phys.* **5** 222–226 ISSN 1745-2481 URL <https://doi.org/10.1038/nphys1198>
- [43] Rickhaus P, Maurand R, Liu M H, Weiss M, Richter K and Schönenberger C 2013 *Nat. Commun.* **4** 2342 ISSN 2041-1723 URL <https://doi.org/10.1038/ncomms3342>
- [44] Rickhaus P, Makk P, Liu M H, Tóvári E, Weiss M, Maurand R, Richter K and Schönenberger C 2015 *Nat. Commun.* **6** 6470 URL <http://www.nature.com/ncomms/2015/150303/ncomms7470/full/ncomms7470.html>
- [45] Grüneis A, Attacalite C, Wirtz L, Shiozawa H, Saito R, Pichler T and Rubio A 2008 *Phys. Rev. B* **78**(20) 205425 URL <https://link.aps.org/doi/10.1103/PhysRevB.78.205425>
- [46] Haddadi F, Wu Q, Kruchkov A J and Yazyev O V 2020 *Nano Lett.* **20** 2410–2415 pMID: 32097013 URL <https://doi.org/10.1021/acs.nanolett.9b05117>
- [47] Tepliakov N V, Wu Q and Yazyev O V 2021 *Nano Letters* **21** 4636–4642 ISSN 1530-6984 URL <https://doi.org/10.1021/acs.nanolett.1c00678>

- [48] Rickhaus P, de Vries F K, Zhu J, Portoles E, Zheng G, Masseroni M, Kurzmann A, Taniguchi T, Watanabe K, MacDonald A H, Ihn T and Ensslin K 2021 *Science* **373** 1257–1260 URL <https://www.science.org/doi/abs/10.1126/science.abc3534>
- [49] Molitor F, Güttinger J, Stampfer C, Graf D, Ihn T and Ensslin K 2007 *Phys. Rev. B* **76**(24) 245426 URL <https://link.aps.org/doi/10.1103/PhysRevB.76.245426>
- [50] Stampfer C, Güttinger J, Molitor F, Graf D, Ihn T and Ensslin K 2008 *Appl. Phys. Lett.* **92** 012102 URL <https://aip.scitation.org/doi/abs/10.1063/1.2827188>
- [51] Liu X, Hao Z, Khalaf E, Lee J Y, Ronen Y, Yoo H, Haei Najafabadi D, Watanabe K, Taniguchi T, Vishwanath A and Kim P 2020 *Nature* **583** 221–225 ISSN 1476-4687 URL <https://doi.org/10.1038/s41586-020-2458-7>
- [52] He M, Li Y, Cai J, Liu Y, Watanabe K, Taniguchi T, Xu X and Yankowitz M 2021 *Nat. Phys.* **17** 26–30 ISSN 1745-2481 URL <https://doi.org/10.1038/s41567-020-1030-6>
- [53] Varlet A, Bischoff D, Simonet P, Watanabe K, Taniguchi T, Ihn T, Ensslin K, Mucha-Kruczyński M and Fal’ko V I 2014 *Phys. Rev. Lett.* **113**(11) 116602 URL <https://link.aps.org/doi/10.1103/PhysRevLett.113.116602>
- [54] Sprinkle M, Siegel D, Hu Y, Hicks J, Tejada A, Taleb-Ibrahimi A, Le Fèvre P, Bertran F, Vizzini S, Enriquez H, Chiang S, Soukiassian P, Berger C, de Heer W A, Lanzara A and Conrad E H 2009 *Phys. Rev. Lett.* **103**(22) 226803 URL <https://link.aps.org/doi/10.1103/PhysRevLett.103.226803>
- [55] Mogera U, Dhanya R, Pujar R, Narayana C and Kulkarni G U 2015 *J. Phys. Chem. Lett.* **6** 4437–4443 URL <https://doi.org/10.1021/acs.jpcllett.5b02145>

# Supplemental Material for Quantum capacitive coupling in large-angle twisted graphene layers

Alina Mreńca-Kolasińska,<sup>1,2,\*</sup> Peter Rickhaus,<sup>3</sup> Giulia Zheng,<sup>3</sup>  
Klaus Richter,<sup>4</sup> Thomas Ihn,<sup>3</sup> Klaus Ensslin,<sup>3</sup> and Ming-Hao Liu (劉明豪)<sup>1,†</sup>

<sup>1</sup>*Department of Physics, National Cheng Kung University, Tainan 70101, Taiwan*

<sup>2</sup>*AGH University of Science and Technology, Faculty of Physics and  
Applied Computer Science, al. Mickiewicza 30, 30-059 Kraków, Poland*

<sup>3</sup>*Solid State Physics Laboratory, ETH Zürich, CH-8093 Zürich, Switzerland*

<sup>4</sup>*Institut für Theoretische Physik, Universität Regensburg, D-93040 Regensburg, Germany*  
(Dated: February 28, 2023)

## I. CARRIER DENSITIES IN DUAL-GATED TWO-LAYER GRAPHENE WITH LINEAR DISPERSION RELATION

### A. Brief review

Here we present the model described in the main text but for a general case of  $N$  gates in the device and including non-zero intrinsic doping. In [? ], a single-layer graphene subject to multiple gates with voltages  $V_1, \dots, V_N$  and arbitrary intrinsic doping  $n_i$  was considered. The carrier density on the graphene sheet can be written as

$$n = n_C + \Delta n \quad (1a)$$

$$n_C = n_i + \sum_{j=1}^N \frac{C_{jG}}{e} V_j + \text{sgn}(n_0) \sqrt{2n_Q |n_i|} \quad (1b)$$

$$\Delta n = \text{sgn}(n_C) n_Q \left( 1 - \sqrt{1 + 2 \frac{|n_C|}{n_Q}} \right) \quad (1c)$$

$$n_Q = \frac{\pi}{2} \left( \frac{\hbar v_F}{e} \sum_{j=1}^N \frac{C_{jG}}{e} \right)^2 \quad (1d)$$

Here, the self-partial capacitance  $C_{jG}$  of the  $j$ th gate can be obtained by numerical electrostatic simulations, and hence contains the position dependence in general:  $C_{jG} = C_{jG}(x, y)$ . This results in position-dependent carrier density profiles:  $n_C = n_C(x, y)$ ,  $n_Q = n_Q(x, y)$ , and the input of doping profile can also be position-dependent as well:  $n_i = n_i(x, y)$ .

In addition to the net carrier density on the considered graphene layer, the “electric potential” on it was also obtained in [? ]:

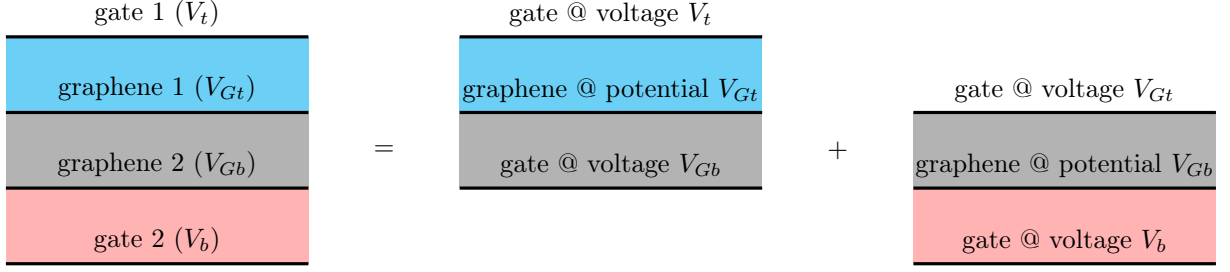
$$V_G = - \frac{\Delta n + \text{sgn}(n_0) \sqrt{2n_Q |n_0|}}{\sum_{j=1}^N \frac{C_{jG}}{e}}. \quad (2)$$

Note that the “gate voltage” actually means the electric potential on the referred metal gate. This means, when two layers of graphene are considered, their electric potential given by Eq. (2) can be treated as a gate voltage to influence the other graphene layer.

### B. Dual-gated decoupled two-layer graphene

The situation we are interested in is sketched in [Figure 1](#). The two graphene layers are decoupled in a way that they still behave like single-layer graphene individually. If they couple, their band structure will be other than the linear dispersion, which is beyond the scope of this work. Note that we assume infinite parallel capacitors and do not care about position dependence here; generalization to include position dependence should be straightforward.

Our main task is to find the carrier densities in the two graphene layers, individually, given top and bottom gate voltages. To be general, we also consider the intrinsic doping  $n_{it}$  and  $n_{ib}$  in the two graphene layers. We apply the formulas (1) and (2) to this problem. The starting point is to treat each graphene layer as a “gate” for the other one:



In this way, the bottom gate (gate 2) do not directly influence graphene layer 1, but due to its modification to the potential of graphene layer 2 which then gates graphene layer 1, gate 2 will indirectly influences graphene layer 1, and similarly as gate 1 to graphene layer 2. In this way, the electric potential on the two graphene layers  $V_{Gt}$  and  $V_{Gb}$  couple each other, and the solution process becomes iterative, in order to make use of the known solutions (1)–(2). This is explained in the following subsections.

### C. Individual dual-gated single-layer graphene

For the graphene layer 1 sketched in Figure 1, we have the classical capacitances  $C_t = \frac{\epsilon_0 \epsilon_t}{d_t}$  for the “top gate” and  $C_G = \frac{\epsilon_0 \epsilon_G}{d_G}$  for the “bottom gate” ( $\epsilon_0$  is the permittivity of free space). If we assume the “bottom gate voltage” to be  $V_{Gb}$ , from Eq. (1) we have :

$$\begin{cases} n_1 = n_{C1} + \Delta n_1 \\ n_{Ct} = n_{it} + \left( \frac{C_t}{e} V_t + \frac{C_G}{e} V_{Gb} \right) + \text{sgn}(n_{it}) \sqrt{2n_{Qt} |n_{it}|} \\ \Delta n_t = \text{sgn}(n_{Ct}) n_{Q1} \left( 1 - \sqrt{1 + 2 \frac{|n_{Ct}|}{n_{Qt}}} \right) \\ n_{Qt} = \frac{\pi}{2} \left( \frac{\hbar v_F}{e} \right)^2 \left( \frac{C_t}{e} + \frac{C_G}{e} \right)^2 \end{cases} \quad (3)$$

for the carrier density and from Eq. (2):

$$V_{Gt} = - \frac{\Delta n_t + \text{sgn}(n_{it}) \sqrt{2n_{Qt} |n_{it}|}}{\frac{C_t}{e} + \frac{C_G}{e}}. \quad (4)$$

for the electric potential. Here, the top gate voltage  $V_t$  is a known input, but the “bottom gate voltage”  $V_{Gb}$  is actually the potential of graphene layer 2, and is unknown.

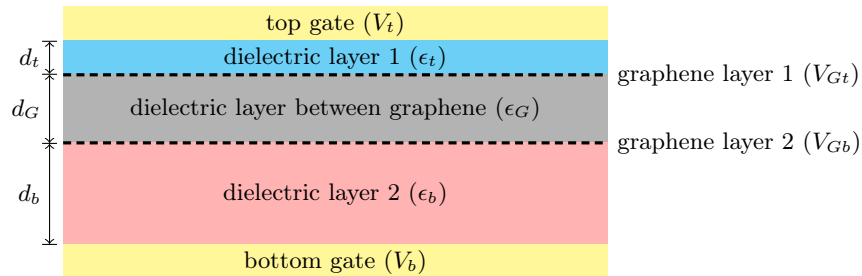


FIG. 1. Dual-gated decoupled two-layer graphene system.

For the graphene layer 2 sketched in **Figure 1**, we have the classical capacitances  $C_G = \frac{\epsilon_0 \epsilon_G}{d_G}$  for the “top gate” and  $C_b = \frac{\epsilon_0 \epsilon_b}{d_b}$  for the “bottom gate”. If we assume the “top gate voltage” to be  $V_{Gt}$ , from Eq. (1) we have:

$$\begin{cases} n_b = n_{Cb} + \Delta n_b \\ n_{Cb} = n_{ib} + \left( \frac{C_b}{e} V_b + \frac{C_G}{e} V_{Gt} \right) + \text{sgn}(n_{ib}) \sqrt{2n_{Qb}|n_{ib}|} \\ \Delta n_b = \text{sgn}(n_{Cb}) n_{Qb} \left( 1 - \sqrt{1 + 2 \frac{|n_{Cb}|}{n_{Qb}}} \right) \\ n_{Qb} = \frac{\pi}{2} \left( \frac{\hbar v_F}{e} \right)^2 \left( \frac{C_b}{e} + \frac{C_G}{e} \right)^2 \end{cases} \quad (5)$$

for the carrier density and from Eq. (2):

$$V_{Gb} = - \frac{\Delta n_b + \text{sgn}(n_{ib}) \sqrt{2n_{Qb}|n_{ib}|}}{\frac{C_b}{e} + \frac{C_G}{e}}. \quad (6)$$

for the electric potential. Here, the bottom gate voltage  $V_b$  is a known input, but the “top gate voltage”  $V_{Gt}$  is actually the potential of graphene layer 1, and is unknown.

#### D. The iteration process

From the above instructions, we can see that the solutions for graphene layer 1 depend on those for graphene layer 2, and vice versa. The iteration process is quite intuitive, and can be done in, for example, the way summarized in **Figure 2**.

#### E. Numerical Example: Decoupled twisted bilayer graphene

For the numerical results presented below  $t = 3$  eV,  $a = \frac{1}{4\sqrt{3}}$  nm,  $\hbar v_F = \frac{3}{2}ta = 0.6495$  nm · eV is adopted. In addition, the intrinsic doping concentrations are taken to be zero for simplicity:  $n_{it} = 0, n_{ib} = 0$ . The iteration solution summarized above can take into account nonzero intrinsic doping straightforwardly.

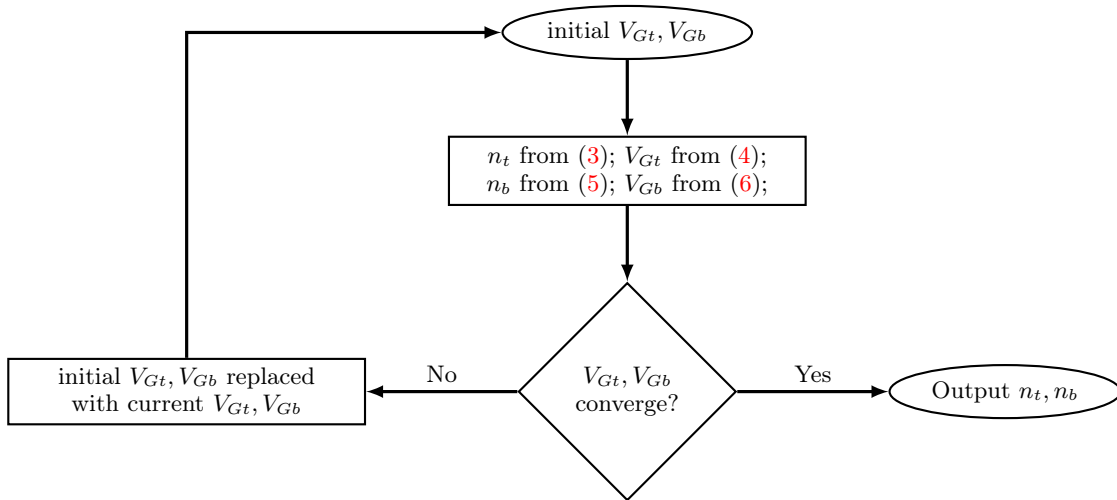


FIG. 2. The iteration process for solving the carrier densities of the two-layer graphene system.



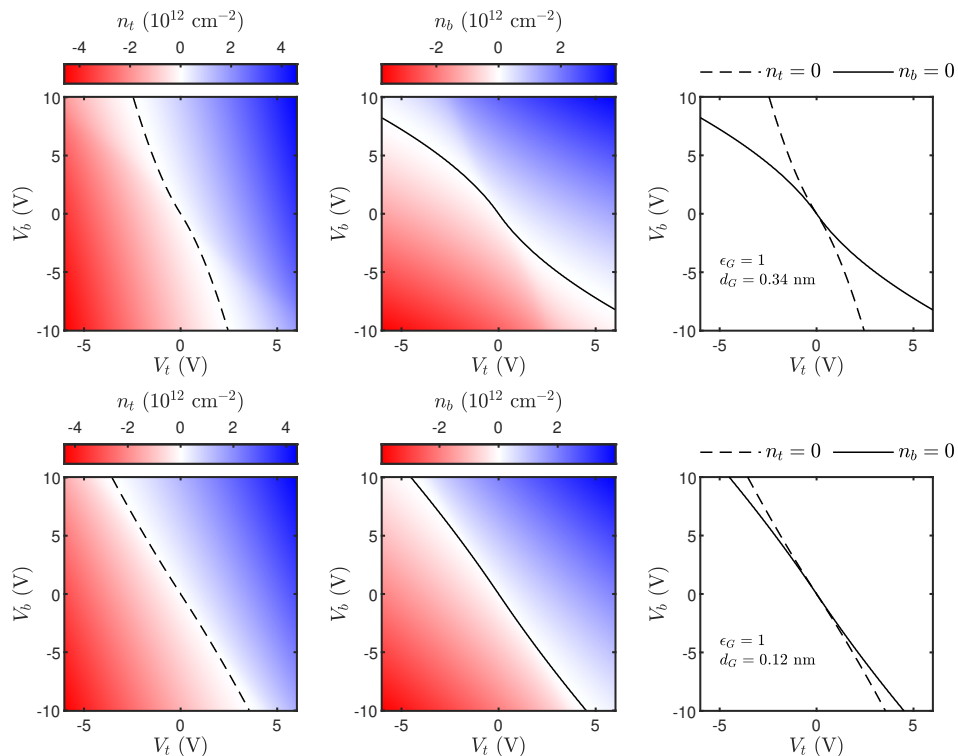


FIG. 3. Numerical example for carrier densities. Upper figures consider  $d_G = 0.34$  nm and lower figures consider  $d_G = 0.12$  nm.

The device we consider a twisted bilayer graphene (tBLG) with a large twist angle that makes the two graphene layers behave as if they are decoupled. The parameters are:

$$\begin{aligned}
 \epsilon_t &= \epsilon_b = \epsilon_{\text{hBN}} = 3.3 \\
 \epsilon_G &= 1.0 \\
 d_t &= 21 \text{ nm} \\
 d_b &= 53 \text{ nm}
 \end{aligned}$$

The thickness  $d_G$  is hard to determine because it is large-angle twisted bilayer graphene sample. If we use the Bernal stacked layer spacing of  $d_G = 0.34$  nm, we get a different result than in the measurement; see the top panel of [Figure 3](#). By using a reduced thickness of  $d_G = 0.12$  nm, the result is shown in the lower panel of [Figure 3](#), and is closer to the experimental result [[?](#)]. Further reducing  $d_G$  will make the two zero density lines get closer and closer to each other. The reduced  $d_G$  is related to the finite electronic thickness of graphene as investigated in Ref. [[?](#)].

### F. Top gate and magnetic field dependence within the linear dispersion relation model

Here we present the result of the quantum transport calculation with the self-consistent electrostatic model based on linear dispersion relation. The calculation was performed for the device with a global backgate and a top gate 320 nm wide, and the capacitance profile is the same as in the main text and in the subsection [IE](#). The measured and calculated transconductance is shown in [Fig. 4](#). Here the theoretical result is clearly different than in the experiment, as the self-consistent model with linear dispersion relation, holds for low magnetic fields only. The main difference with respect to the map presented in [Fig. 3](#) of the main text is the absence of the kinks at the crossings of the LLs. The theoretical results in [Fig. 3](#) of the main text were obtained with the model developed taking into account the Landau quantization, described in the [Section II](#). Nevertheless, for low magnetic field this model gives satisfactory results, and the Fabry-Pérot oscillations occurring at above  $V_t = 3.7$  V are recovered with a great precision.

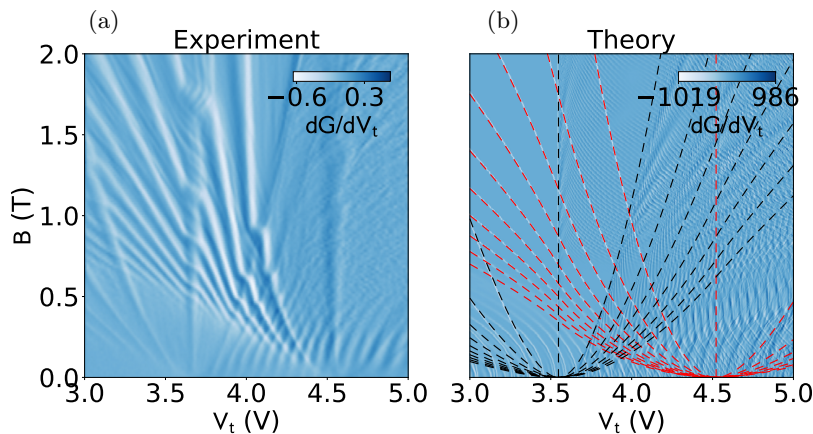


FIG. 4. The numerical derivative of the (a) experimental and (b) calculated two-terminal conductance as a function of top gate voltage and magnetic field obtained at  $V_b = -10$  V for a dual-gated tBLG for the Dirac linear dispersion relation model. The dashed lines in (b) show the Landau levels calculated for the upper layer (black lines) and lower layer (red lines).

## II. CARRIER DENSITIES IN DUAL-GATED TWO-LAYER GRAPHENE IN STRONG EXTERNAL MAGNETIC FIELD

The linear dispersion electrostatic model can be used to accurately describe the transport phenomena in low magnetic field, however the Landau quantization is important at larger fields. In this section we present the electrostatic model for the quantum capacitance with the Landau levels taken into account through the density of states (DOS). This approach is based on the quantum capacitance model [?] developed for the linear dispersion relation. However, contrary to Ref. [?], no analytical solution for the carrier density and electrostatic potential are attempted; instead we calculate them numerically, as explained in the following subsection.

### A. Carrier density

We consider the problem for non-zero transverse magnetic field  $B_z$ . The Landau level (LL) spectrum is described by

$$E_{n_L} = \text{sgn}(n_L) \sqrt{2eB_z \hbar v_F^2 |n_L|}, \quad n_L = 0, \pm 1, \pm 2, \dots \quad (7)$$

The carrier density in zero temperature limit is given by

$$n(E, B_z) = \int_0^E D(E', B_z) dE', \quad (8)$$

where  $D(E, B_z)$  is the density of states. In infinite pristine graphene the DOS can be written as

$$D(E, B_z) = \frac{4eB_z}{h} \sum_{n_L} \delta(E - E_{n_L}), \quad (9)$$

where  $E_{n_L}$  is given by Eq. (7). In real systems the  $\delta$  peaks of DOS at Landau energies are broadened due to the presence of disorder, phonons or impurities. We take this smoothing of DOS into account in a phenomenological way using the approximation of the Dirac's delta by the Lorentzian function  $f(E) = \frac{1}{\pi} \frac{\epsilon}{\epsilon^2 + E^2}$  with the width  $\epsilon$ , which in the limit of small  $\epsilon$  is the  $\delta$  function

$$\lim_{\epsilon \rightarrow 0} \frac{1}{\pi} \frac{\epsilon}{\epsilon^2 + E^2} = \delta(E). \quad (10)$$

Using this expression, we can calculate the carrier density exactly:

$$n(E, B_z) = \frac{4eB_z}{h} \frac{1}{\pi} \sum_{n_L} \int_0^E \frac{\epsilon}{\epsilon^2 + (E' - E_{n_L})^2} dE' \quad (11)$$

$$= \frac{4eB_z}{h} \frac{1}{\pi} \sum_{n_L} \left[ \arctan \left( \frac{E - E_{n_L}}{\epsilon} \right) \right]_0^E \quad (12)$$

$$= \frac{4eB_z}{h\pi} \sum_{n_L} \left[ \arctan \left( \frac{E - E_{n_L}}{\epsilon} \right) + \arctan \left( \frac{E_{n_L}}{\epsilon} \right) \right]. \quad (13)$$

The parameter  $\epsilon$  is a knob that can be used to adjust the broadening of LLs, for example to fit best the experiment. A representative plot of  $n(E, B_z)$  for  $\epsilon = 0.4$  meV and a cross-section for  $B_z = 0.6$  T are presented in Fig. 5. If there is no external gating, but an intrinsic doping  $n_0$  is present, the quasi-Fermi level  $E_0$  is described by

$$n_0 = \frac{4eB_z}{h\pi} \sum_{n_L} \left[ \arctan \left( \frac{E_0 - E_{n_L}}{\epsilon} \right) + \arctan \left( \frac{E_{n_L}}{\epsilon} \right) \right], \quad (14)$$

which can be solved numerically to find  $E_0$ .

### B. Quantum capacitance model, general expressions

The starting point are the formulas describing the carrier density in terms of the self-partial capacitances [? ]. The net electron number density on graphene is

$$n_G = \frac{\rho_G}{-e} = \sum_{j=1}^N C_{jG} (V_j - V_G) / e, \quad (15)$$

where  $C_{jG}$  is the self-partial capacitance of the  $j$ th gate, which can, in general, be position-dependent. If there is a non-zero intrinsic charge density  $n_0$  on graphene, the net carrier density of graphene is given by  $n = n_0 + n_G$ , which should equal the density given by Eq. (13), i.e.  $n_0 + n_G = n(E_0 + eV_G)$ . Thus we obtain the equation

$$\sum_{j=1}^N C_{jG} (V_j - V_G) / e + n_0 = \frac{4eB_z}{h\pi} \sum_{n_L} \left[ \arctan \left( \frac{E_0 + eV_G - E_{n_L}}{\epsilon} \right) + \arctan \left( \frac{E_{n_L}}{\epsilon} \right) \right]. \quad (16)$$

Here the  $V_G$  value can be found numerically.

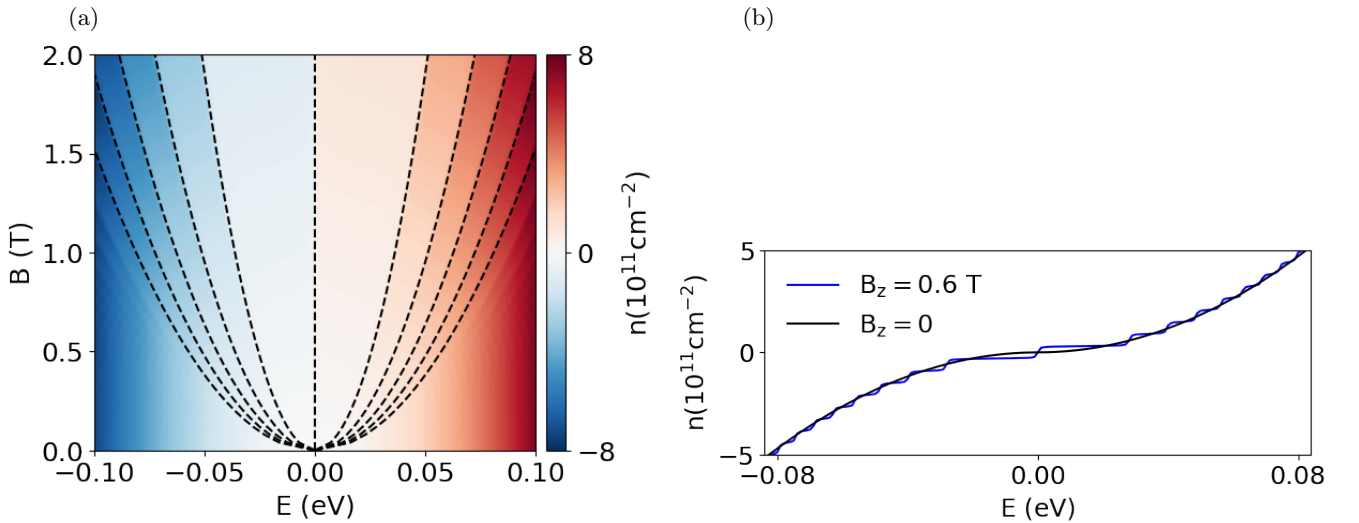


FIG. 5. (a) Density obtained for  $\epsilon = 0.4$  meV. (b) Cross-section for  $B_z = 0.6$  T and  $B_z = 0$ .

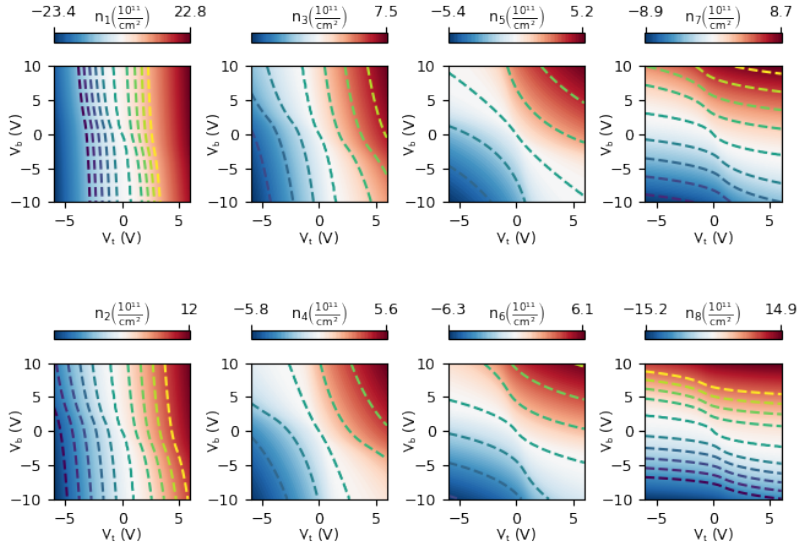


FIG. 6. The layer densities calculated for 8-layer graphene.

### C. Iterative process for two decoupled graphene layers

For the two decoupled, but electrostatically coupled graphene layers with nonzero magnetic field, we use a similar approach as in the zero-field case, following the algorithm in Fig. 2, but instead of closed formulas (3-6) we calculate  $V_{Gt}$  and  $V_{Gb}$  numerically from Eq. (16).

## III. DECOUPLED $n$ -LAYER GRAPHENE

Next we consider a the case of  $n$  stacked layers of graphene, each layer with a large relative twist angle with respect to the closest layers, such that the nearest neighboring layers are decoupled. We assume that the next neighboring layers are also decoupled, regardless of their relative twist angle. The self-consistent method as described in Section I is easily extended to  $n$  layers. Each layer is effectively gated from the top and bottom by an adjacent gate or graphene layer, and the iteration is performed until the electric potential  $V_{Gi}$ ,  $i = 1, 2, \dots, n$  in all the layers converge to the required tolerance.

Fig. 6 shows example of the densities calculated for 8 layers of graphene dual gated by infinite gates, with the top and bottom gates separated from the  $n$ -layer graphene by  $d_t = 21$  nm and  $d_b = 53$  nm of hBN, respectively. We can see that the topmost layer density  $n_1$  depends very weakly on the back gate voltage  $V_b$ , while the lowest layer density  $n_8$  depends weakly on the top gate voltage  $V_t$ . The middle layers labeled by 4 and 5 are partially screened by the outer layers, thus the densities  $n_4$  and  $n_5$  are on average lower than the outer layers; moreover, the density in the bipolar region is close to zero.

Fig. 7 shows the densities of the topmost, bottom most graphene layer, and the middle layer (for odd  $n$ ) as a function of the number of layers  $n$ , at selected voltage configurations. The value of the density saturates as the number of layers increases. For the middle layer the value saturates at a value close to zero.

## IV. QUANTUM CAPACITANCE MODEL FOR DUAL-GATED BERNAL STACKED BILAYER GRAPHENE

The relation between the carrier density and external gates voltage is often described in the classical capacitance model (see [? ]). Within this simple approach, the densities of the top and bottom layers are related to  $V_t$  and  $V_b$  using the parallel capacitor model. Then the asymmetry parameter is calculated in accordance with Ref. [? ], and with that the band offset is obtained. All of these quantities can in general be position-dependent. Details are explained in Refs. [? ? ].

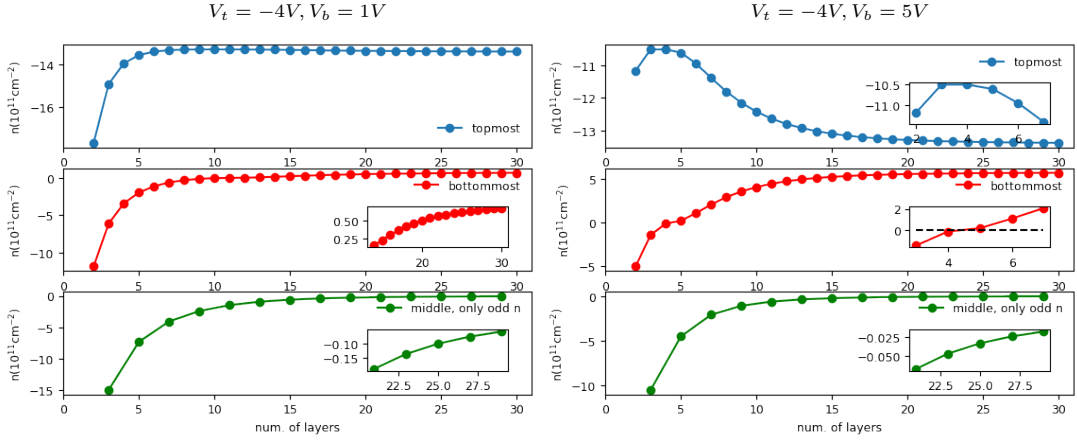


FIG. 7. The top, bottom, and middle layer densities as a function of the number of stacked layers. The origin of the nonmonotonic behaviour for  $(V_t, V_b) = (-4, 5)V$  is unknown.

However, when graphene is doped with additional charge, it leads to the shift of the Fermi energy. Thus the electric potential difference between a gate and graphene is smaller than the applied gate voltage. This phenomenon can be described in terms of the quantum capacitance which is connected in series to the classical capacitance. Here we introduce a model for the Bernal stacked bilayer graphene that takes into account the potential energy that the charge carriers gain.

### A. Tight-binding model for bilayer graphene

We consider the atomistic tight-binding model Hamiltonian

$$H = \sum_{i,j} (t_{ij} c_i^\dagger c_j + H.c.) + \sum_i V_i c_i^\dagger c_i \quad (17)$$

including the intralayer nearest-neighbor hopping  $t_{ij} = t$  and interlayer hopping  $t_{ij} = \gamma_1$  between the dimer sites, and the on-site energy is

$$V_i = \begin{cases} U_0 + U/2 = -e\phi_t, & \text{top} \\ U_0 - U/2 = -e\phi_b, & \text{bottom} \end{cases}, \quad (18)$$

where  $U$  is the asymmetry parameter and  $U_0$  is the band offset.

### B. Relation between the carrier density and the electric potential

As derived in [? ], the carrier density of the individual graphene layers is given by

$$n_{t,b} \approx \frac{n}{2} \pm \frac{n_\perp U}{4\gamma_1} \ln \left( \frac{|n|}{2n_\perp} + \frac{1}{2} \sqrt{\left(\frac{n}{n_\perp}\right)^2 + \left(\frac{U}{2\gamma_1}\right)^2} \right), \quad (19)$$

To write the equations in a clearer way, we can define the capacitances

$$C_t/e = \frac{\epsilon_t \epsilon_0}{ed_t}, \quad (20)$$

$$C_b/e = \frac{\epsilon_b \epsilon_0}{ed_b}, \quad (21)$$

$$C_g/e = \frac{\epsilon_g \epsilon_0}{ed}, \quad (22)$$

that are defined in Fig. 8. It is possible to describe how the carrier density and the asymmetry parameter are related to the gate potentials. We can use the following formulas for the electron densities

$$n_t = \frac{C_t}{e} (V_t - \phi_t) + \frac{C_g}{e} (\phi_b - \phi_t) \quad (23)$$

$$n_b = \frac{C_b}{e} (V_b - \phi_b) + \frac{C_g}{e} (\phi_t - \phi_b). \quad (24)$$



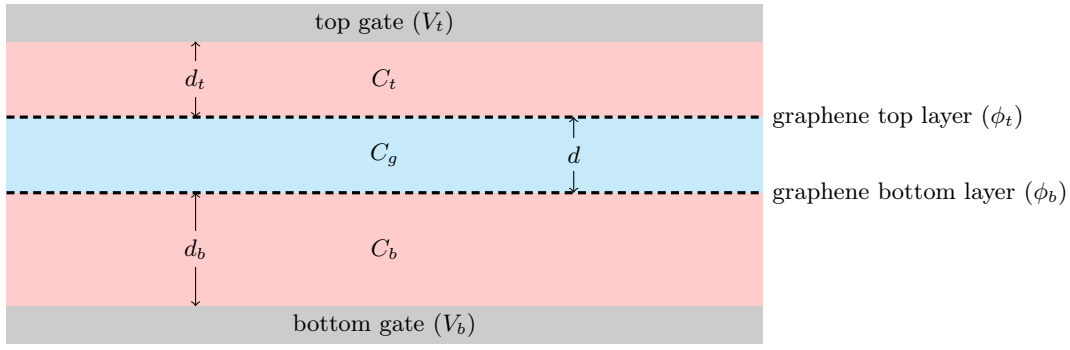


FIG. 8. Dual-gated Bernal stacked BLG.

where  $-e\phi_t = U_0 + \frac{U}{2}$  and  $-e\phi_b = U_0 - \frac{U}{2}$ . Substituting  $\phi_t = \frac{U_0}{-e} + \frac{U}{-2e}$  and  $\phi_b = \frac{U_0}{-e} - \frac{U}{-2e}$ , and  $\frac{U_0}{-e} = V_G$ , we get

$$n_t = \frac{C_t}{e} \left[ V_t - \left( V_G - \frac{U}{2e} \right) \right] + \frac{C_g}{e} \frac{U}{e}, \quad (25)$$

$$n_b = \frac{C_b}{e} \left[ V_b - \left( V_G + \frac{U}{2e} \right) \right] - \frac{C_g}{e} \frac{U}{e}, \quad (26)$$

The relation between the carrier density, the asymmetry parameter, and the band offset is given by [? ]

$$-eV_G = -\text{sgn}(n) \sqrt{\frac{\gamma_1^2}{2} + \frac{U^2}{4} + \hbar^2 v_F^2 \pi |n| - \frac{\gamma_1}{2} \sqrt{\gamma_1^2 + (2\hbar v_F)^2 \pi |n|} \left( 1 + \frac{U^2}{\gamma_1^2} \right)} \quad (27)$$

Equations (19, 25-27) describe the relation between the four unknown quantities  $n_t$ ,  $n_b$ ,  $U$ , and  $V_G$ . To solve the problem we rewrite the equations in terms of independent quantities  $n_t - n_b$ ,  $n = n_t + n_b$ ,  $U$ , and  $V_G$  [? ]. From Eq. (19), we get

$$n_b - n_t = -\frac{n_{\perp} U}{2\gamma_1} \ln \left( \frac{|n|}{2n_{\perp}} + \frac{1}{2} \sqrt{\left( \frac{n}{n_{\perp}} \right)^2 + \left( \frac{U}{2\gamma_1} \right)^2} \right). \quad (28)$$

On the other hand, from Eqs. (25) and (26), we obtain

$$n_b - n_t = \frac{C_b}{e} \left[ V_b - \left( V_G + \frac{U}{2e} \right) \right] - \frac{C_t}{e} \left[ V_t - \left( V_G - \frac{U}{2e} \right) \right] - \frac{2C_g}{e} \frac{U}{e}. \quad (29)$$

Adding up Eqs. (25) and (26)

$$n = n_b + n_t = \frac{C_b}{e} V_b + \frac{C_t}{e} V_t - \frac{C_b + C_t}{e} V_G + \frac{C_t - C_b}{e} \frac{U}{2e}. \quad (30)$$

We obtain a system of four nonlinear equations (27 - 30) coupling four independent variables. We can solve them numerically (using numerical methods for the solution of systems of nonlinear equations). Their values allow for the calculation of the onsite potential that is inserted into the tight-binding Hamiltonian.

### C. Application for transport

As an example of the application of the potential profile for transport we consider Bernal stacked bilayer graphene (BLG) gated by a global bottom gate and finite top gate which creates a position dependent density profile in BLG. Depending on the gate voltage, the system can be tuned to unipolar (nn'n or pp'p) or bipolar (np'n or pn'p) regime. For the calculation we use the model from Ref. [? ] applied to the tight binding wave function matching method on a zigzag nanoribbon with the scaling factor  $s_f = 2$ .

The transconductance map as a function of top gate and backgate voltages is shown in Fig. 9(a). The map is divided into 4 regions of different polarities combinations, marked in Fig. 9(a). In the bipolar regime, the FP oscillations are seen parallel to the  $n = 0$  axis. The white lines are calculated from the condition  $\Delta\phi = 2\Delta k L_c = 2\pi$ , being in a good agreement with the oscillations.

Fig. 9(b) shows the conductance as a function of the top gate voltage and magnetic field at  $V_b = 1$  V.

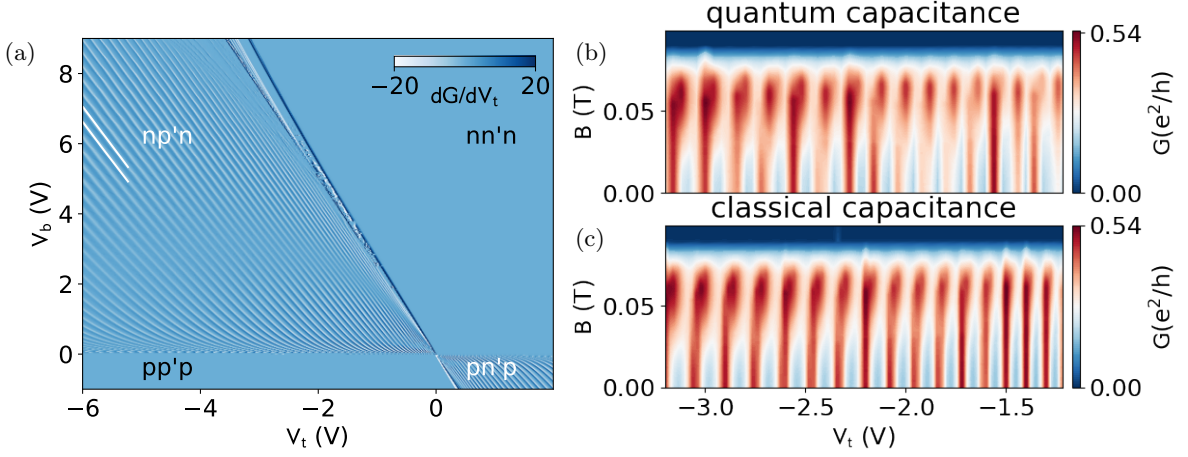


FIG. 9. (a) Conductance as a function of top and bottom gate voltage obtained for a dual-gated bilayer graphene using the quantum capacitance model. The white lines show the expected direction of the fringes calculated from the condition  $\Delta\phi = 2\Delta kL_c = 2\pi$ . (b) Conductance as a function of top gate voltage and magnetic field at  $V_b = 1$  V using the quantum capacitance model. (c) Same result using the classical model.

## V. DUAL-GATED TWISTED DOUBLE BILAYER GRAPHENE

The approach we use for the twisted double bilayer graphene (tdBLG) is based on the quantum capacitance model described in Section IV B. In case of two electrostatically coupled BLG, each of the layers is gated by an adjacent gate or graphene layer. Therefore, we modify the equations developed for a single BLG, Eqs. (27 - 30) with the input of an adequate electric potential or gate voltage, and obtain a system of eight coupled equations describing the carrier densities and the potentials for the two bilayers. The scheme of the dual-gated tdBLG is shown in Fig. 10.

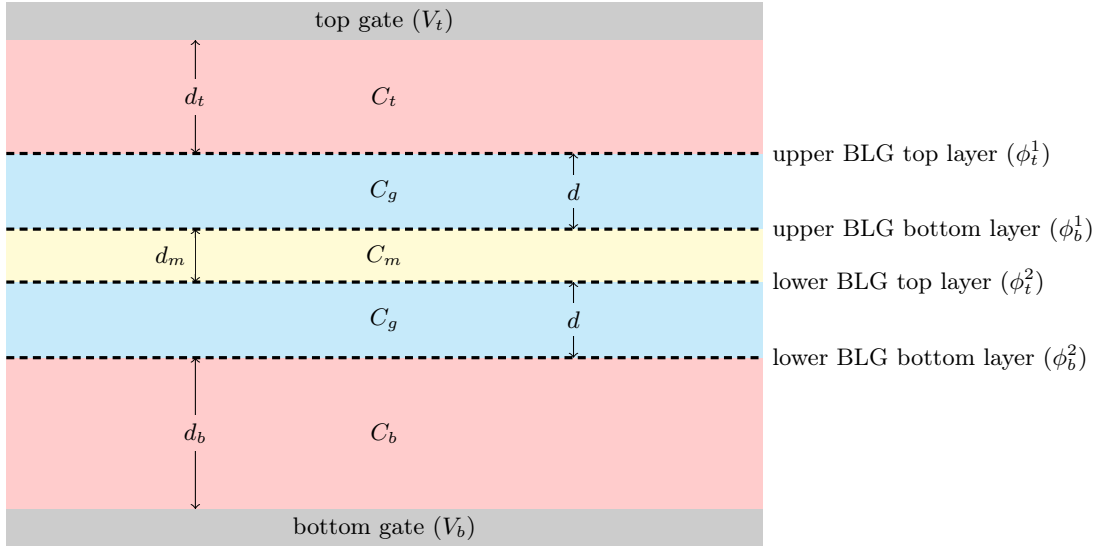


FIG. 10. Dual-gated Bernal stacked BLG.

We can define the capacitances

$$C_t/e = \frac{\epsilon_t \epsilon_0}{e d_t}, \quad (31)$$

$$C_b/e = \frac{\epsilon_b \epsilon_0}{e d_b}, \quad (32)$$

$$C_g/e = \frac{\epsilon_g \epsilon_0}{e d}, \quad (33)$$

$$C_m/e = \frac{\epsilon_m \epsilon_0}{e d_m}. \quad (34)$$

In this case, we label the upper bilayer by 1 and the lower bilayer by 2, and within each bilayer, the top layer is labeled by a subscript  $t$ , and bottom layer – by a subscript  $b$ . We can use the following formulas for the electron densities

$$n_{1,t} = \frac{C_t}{e} (V_t - \phi_{1,t}) + \frac{C_g}{e} (\phi_{1,b} - \phi_{1,t}), \quad (35)$$

$$n_{1,b} = \frac{C_r}{e} (\phi_{2,t} - \phi_{1,b}) + \frac{C_g}{e} (\phi_{1,t} - \phi_{1,b}), \quad (36)$$

$$n_{2,t} = \frac{C_r}{e} (\phi_{1,b} - \phi_{2,t}) + \frac{C_g}{e} (\phi_{2,b} - \phi_{2,t}), \quad (37)$$

$$n_{2,b} = \frac{C_b}{e} (V_b - \phi_{2,b}) + \frac{C_g}{e} (\phi_{2,t} - \phi_{2,b}). \quad (38)$$

where  $-e\phi_{i,t} = U_{i,G} + \frac{U_i}{2}$  and  $-e\phi_{i,b} = U_{i,G} - \frac{U_i}{2}$ . Substituting  $\frac{U_{i,G}}{-e} = V_{i,G}$ , we get  $\phi_{i,t} = V_{i,G} + \frac{U_i}{-2e}$  and  $\phi_{i,b} = V_{i,G} - \frac{U_i}{-2e}$ .

We rewrite equations (27 - 28) developed for an individual BLG and equations (35 - 38) in terms of eight independent quantities  $n_{i,b} - n_{i,t}$ ,  $n_i = n_{i,t} + n_{i,b}$ ,  $U_i$ , and  $V_{i,G}$  in the two decoupled BLGs. In this way, we can also include in the model the intrinsic doping  $n_{0,i}$  and the density imbalance between bottom and top layer within a BLG  $\Delta n_{0,i} = n_{0,i,b} - n_{0,i,t}$ . After a few rearrangements we get:

$$-eV_{i,G} = -\text{sgn}(n_i) \sqrt{\frac{\gamma_1^2}{2} + \frac{U_i^2}{4} + \hbar^2 v_F^2 \pi |n_i| - \frac{\gamma_1}{2} \sqrt{\gamma_1^2 + (2\hbar v_F)^2 \pi |n_i|} \left(1 + \frac{U_i^2}{\gamma_1^2}\right)}, \quad i = 1, 2, \quad (39)$$

$$n_{i,b} - n_{i,t} = -\frac{n_{\perp} U_i}{2\gamma_1} \ln \left( \frac{|n_i|}{2n_{\perp}} + \frac{1}{2} \sqrt{\left(\frac{n_i}{n_{\perp}}\right)^2 + \left(\frac{U_i}{2\gamma_1}\right)^2} \right), \quad i = 1, 2. \quad (40)$$

$$n_{1,b} - n_{1,t} = \frac{C_m}{e} \left[ V_{2,G} - \frac{U_2}{-2e} - \left( V_{1,G} + \frac{U_1}{2e} \right) \right] - \frac{C_t}{e} \left[ V_t - \left( V_{1,G} - \frac{U_1}{2e} \right) \right] - \frac{2C_g}{e} \frac{U_1}{e} + \Delta n_{0,1}, \quad (41)$$

$$n_{2,b} - n_{2,t} = \frac{C_b}{e} \left[ V_b - \left( V_{2,G} + \frac{U_2}{2e} \right) \right] - \frac{C_m}{e} \left[ V_{1,G} + \frac{U_1}{-2e} - \left( V_{2,G} - \frac{U_2}{2e} \right) \right] - \frac{2C_g}{e} \frac{U_2}{e} + \Delta n_{0,2}. \quad (42)$$

$$n_1 = n_{1,b} + n_{1,t} = \frac{C_m}{e} \left[ V_{2,G} - \frac{U_2}{-2e} - \left( V_{1,G} + \frac{U_1}{2e} \right) \right] + \frac{C_t}{e} \left[ V_t - \left( V_{1,G} - \frac{U_1}{2e} \right) \right] + n_{0,1}, \quad (43)$$

$$n_2 = n_{2,b} + n_{2,t} = \frac{C_b}{e} \left[ V_b - \left( V_{2,G} + \frac{U_2}{2e} \right) \right] + \frac{C_m}{e} \left[ V_{1,G} + \frac{U_1}{-2e} - \left( V_{2,G} - \frac{U_2}{2e} \right) \right] + n_{0,2}. \quad (44)$$

In this approach we solve the system of eight equations (39 - 44) numerically. Since this method assumes that the system is conducting, in the insulating case which is beyond the current model, the solution cannot be found. It is equivalent to the Fermi energy falling within the bandgap, preventing the transport, which we interpret as a gapped system.

The density imbalance between a BLG bottom and top layer can be estimated from the displacement field needed to close the gap in the  $i$ th BLG  $D_i = -e\Delta n_{0,i}/2\epsilon_0$ . For example, in Ref. [?] the measured displacement field which closed the gap in the top layer 0.12 V/nm gives  $\Delta n_{0,1} = -13 \times 10^{11} \text{ cm}^{-2}$ .

## VI. GATED TWO-LAYER MATERIAL WITH A GENERAL BAND STRUCTURE

Here we consider a two-layer material with a general band structure, hence no analytical solution for the carrier density and electrostatic potential is derived. This is a purely numerical approach, including the calculation of the density of states (DOS). However, for specific materials some of the intermediate steps can be done analytically to speed up the calculation.

### A. Density of states and the carrier density

We start the calculation with a general band structure  $E(\mathbf{k})$ . One of the ways to calculate the DOS is a numerical integration using the definition

$$D(E) = \frac{4}{L^2} \left( \frac{L}{2\pi} \right)^2 \int \delta(E - E(\mathbf{k})) d^2k, \quad (45)$$

where the Dirac delta  $\delta(E - E(\mathbf{k}))$  can be approximated e.g. by a Lorentzian function

$$\delta(E) \approx \frac{1}{\pi} \frac{\epsilon}{\epsilon^2 + E^2}. \quad (46)$$

Next, the carrier density in the zero temperature limit is calculated as the integral

$$n(E) = \int_0^E D(E') dE'. \quad (47)$$

Both integrals can be done numerically using standard quadrature available e.g. in numerical libraries. The flow is as in Fig. 11.

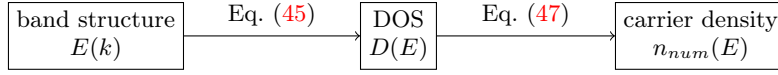


FIG. 11. The density calculation for an arbitrary band structure.

The density can be then stored in an array and used for the quantum capacitance model. Note that in such case it can be stored for discrete values of  $E = E_j, j = 0, 1, \dots$ ; we denote the density obtained by such numerical integration by  $n_{num}(E_j)$ . The density for an arbitrary energy can be then calculated by interpolation.

For the two decoupled layers, we then use the self-consistent approach presented in Fig. 2, with the  $n_1, n_2$  substituted by the numerically calculated  $n_{num}(E)$  in place of the analytical ones, and  $V_{G1}, V_{G2}$  are calculated solving equation (15) numerically.

### B. Examples

As an example, we can consider a monolayer graphene and compare the result to the one obtained with the analytical approach instead of the numerical one. Fig. 12(a) shows the density as a function of energy, for a zero intrinsic doping  $n_0 = 0$ , as well as the analytical result, given by  $n(E) = \text{sgn}(E) \frac{1}{\pi} \left( \frac{E}{\hbar v_F} \right)^2$ . The numerical calculation was done with Dirac delta approximated by a Lorentzian function (46) with  $\epsilon = 4 \cdot 10^{-5}$  eV.

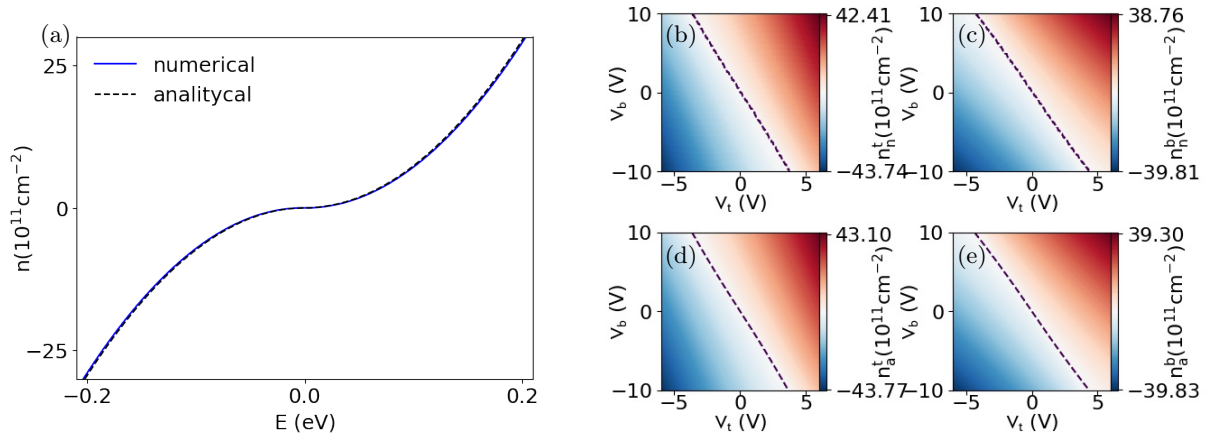


FIG. 12. (a) Carrier density as a function of energy. (b-e) Densities on top and bottom graphene layer as a function of top gate and backgate voltage for (b, c) a numerical calculation and (d, e) an analytical solution with the linear dispersion relation model.